

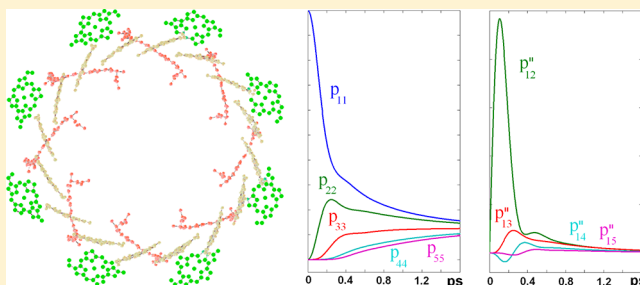
# Spectra and Dynamics in the B800 Antenna: Comparing Hierarchical Equations, Redfield and Förster Theories

Vladimir Novoderezhkin<sup>\*,†</sup> and Rienk van Grondelle<sup>‡</sup>

<sup>†</sup>A. N. Belozersky Institute of Physico-Chemical Biology, Moscow State University, Moscow, Russia

<sup>‡</sup>Department of Physics and Astronomy, Faculty of Sciences, VU University Amsterdam, Amsterdam, The Netherlands

**ABSTRACT:** We model the spectra (absorption and circular dichroism) and excitation dynamics in the B800 ring of the LH2 antenna complex from *Rs. molischianum* using different theoretical approaches, i.e., Förster theory, standard and modified versions of the Redfield theory, and the more versatile nonperturbative approach based on hierarchically coupled equations for the reduced density operator. We demonstrate that, although excitations in the B800 ring are localized due to disorder, thermal effects, and phonons, there are still sizable excitonic effects producing shift, narrowing, and asymmetry of the spectra. Moreover, the excitation dynamics reveals the presence of long-lived (up to 1 ps) non-oscillatory coherences between the exciton states maintained due to nonsecular population-to-coherence transfers. The sub-ps decay of the coherences is followed by slow motion of the excitation around the ring, producing equilibration of the site populations with a time constant of about 3–4 ps, which is slower than the B800 → B850 transfer. The exact solution obtained with the hierarchical equations is compared with other approaches, thus illustrating limitations of the Förster and Redfield pictures.



## 1. INTRODUCTION

The light-harvesting complex LH2 from purple photosynthetic bacteria consists of two highly symmetric rings of bacteriochlorophyll (BChl) molecules: the inner ring of 18 (16) tightly packed BChl's absorbing around 850 nm (B850 band) and the outer ring of 9(8) weakly interacting BChl's with an absorption maximum near 800 nm (B800 band).<sup>1–3</sup> The energy transfer dynamics includes migration of excitations around the B800 ring, superimposed on the transfer to exciton states of the B850 ring (for a review, see refs 4–6). The possible interplay of intraband B800 → B800 and interband B800 → B850 energy transfer has been the subject of intense studies by hole burning,<sup>7–12</sup> pump–probe,<sup>13–23</sup> three-pulse photon echo,<sup>24,25</sup> and two-dimensional (2D) photon echo techniques<sup>26</sup> together with theoretical modeling.<sup>26–29</sup>

The isotropic transient absorption (TA) kinetics in the 800 nm region exhibits a biexponential decay.<sup>14–23</sup> According to earlier interpretations, the slow (1.2–1.9 ps) component has been assigned to the B800 → B850 transfers, whereas the fast (0.3–0.8 ps) component has been taken to reflect the hopping of localized excitations around the B800 ring. The TA anisotropy near 800 nm decays with approximately the same (0.3–0.5 ps) time constant, apparently supporting the idea of fast hopping-type migration around the B800 ring giving rise to depolarization. However, this intuitive picture (neglecting excitonic effects and implying incoherent migration within the B800 band) is not supported by quantitative modeling. Due to the isoenergetic character of the BChl's excited states, even weak coupling between them creates sizable excitonic

coherences (not destroyed by the disorder) that should be taken into account in order to reproduce the absorption (OD),<sup>30</sup> circular dichroism (CD),<sup>31</sup> polarized pump–probe kinetics,<sup>29</sup> and the shape of the 2D photon echo spectra<sup>26</sup> observed within the B800 band.

Modeling performed with the standard Redfield theory has led to a detailed picture of the energy transfers in the B800 ring (as well as in the whole B800–B850 antenna) based on a quantitative fit of the measured TA kinetics.<sup>29</sup> It has been shown that impulsive excitation creates coherences between the B800 states, that decay with a time constant of 0.3–0.5 ps, producing a fast decay of the TA anisotropy from 0.4 to 0.2. This is followed by a slow migration around the B800 ring with a time constant of several ps producing further depolarization from 0.2 to 0.1. Thus, it has been demonstrated that the fast sub-ps component of the anisotropy decay does not reflect any population migration at all but is connected with the coherence dynamics. The population equilibration within the B800 ring occurs in the ps time scale, being even slower than the interband B800 → B850 energy transfer.<sup>29</sup>

A recent 2D photon echo study of the B800–820 complex<sup>26</sup> has revealed the presence of excitonic effects within the B800 band, thus confirming earlier suggestions.<sup>29,30</sup> The dynamics within the B800 band indicates that there is no significant

**Special Issue:** Rienk van Grondelle Festschrift

**Received:** January 28, 2013

**Revised:** March 25, 2013

intraband B800  $\rightarrow$  B800 transfer on a time scale preceding the interband B800  $\rightarrow$  B850 transfer, as suggested by polarized TA modeling.<sup>29</sup>

In this paper, we wish to revisit the excitation dynamics within the B800 ring using a recently developed physical approach based on the hierarchically coupled equations of motion for the density operator.<sup>32,33</sup> This method allows a realistic description of the energy transfer where the coupling of electronic excitations with phonon reorganization dynamics is taken into account in a nonperturbative manner. Such an approach has been used to model the coherent dynamics in the FMO complex,<sup>33–37</sup> in the B850 band of the LH2 complex,<sup>38,39</sup> dynamics within the LH1–RC core complex,<sup>40</sup> energy transfer between two B850 rings,<sup>38</sup> and transfers between the B850 and LH1(B875) rings.<sup>41</sup> In the present study, we model the linear spectra and one-exciton dynamics in the B800 band of LH2 antenna at 77 K using the hierarchical equations, different versions of the Redfield approach, and the Förster theory.

## 2. METHODS

We model the B800 ring of purple bacterium *Rhodospirillum* (Rs.) *molischianum*, containing  $N = 8$  BChl 800 molecules, using the structure reported by Koepke et al.<sup>2</sup> The one-exciton Hamiltonian in the site representation is

$$H = \sum_{j=1}^N \omega_{j0} |j\rangle \langle j| + \sum_{j \neq j'}^N M_{jj'} |j\rangle \langle j'| \quad (1)$$

where  $\omega_{j0} = \omega_{j0}^0 + \lambda_j$  is the energy of the Franck–Condon transition of the  $j$ th site (including the zero-phonon energy  $\omega_{j0}^0$  and reorganization energy  $\lambda_j$ ),  $M_{jj'}$  is the interaction energy between the  $j$ th and  $j'$ th sites. The coupling between nearest neighboring BChl's 800 was estimated as  $M = -19 \text{ cm}^{-1}$  according to calculations assuming that the complex is in a dielectric medium<sup>42</sup> or  $M = -14$  to  $-27 \text{ cm}^{-1}$  according to earlier calculations for the isolated complex (see Table 2 in ref 42). According to this data we assume a nearest neighbor coupling of  $M = -20 \text{ cm}^{-1}$  and neglect other couplings. The site energies  $\omega_{j0}$  are supposed to be the same for all the sites (the  $\omega_{j0} = 12590 \text{ cm}^{-1}$  value is used in order to reproduce the absorption peak position).

The coupling of the  $j$ th electronic transition to phonons is described by the spectral density:

$$C_j(\omega) = 2\lambda_j \frac{\omega \gamma_j}{\omega^2 + \gamma_j^2} \quad (2)$$

with reorganization energy  $\lambda_j$  and damping constant  $\gamma_j$ . These parameters have been adjusted from the fit of linear spectra giving  $\lambda_j = 25 \text{ cm}^{-1}$  and  $\gamma_j = 35 \text{ cm}^{-1}$  (supposing that they are the same for all the sites). In our model, the phonons acting on different sites are uncorrelated. We also neglect off-diagonal coupling, i.e., modulation of the interaction energies  $M_{jj'}$  by the phonons. The excited state dynamics for such a model can be described by the hierarchically coupled equations of motion derived by Ishizaki and Fleming.<sup>32,33</sup> The matrix elements of the reduced density operator corresponding to the site populations and coherences between the sites are given by

$$\begin{aligned} \dot{\sigma}_{ij}^n &= -(\gamma^n + i\omega_{ij})\sigma_{ij}^n - i \sum_m (M_{im}\sigma_{mj}^n - \sigma_{im}^n M_{mj}) \\ &\quad + i(\lambda_i \sigma_{ij}^{n_i+} - \sigma_{ij}^{n_i+} \lambda_j) + i(\gamma_{\theta-}^n \sigma_{ij}^{n_i-} - \sigma_{ij}^{n_i-} \gamma_{\theta+}^n) \\ \gamma^n &= \sum_m n_m \gamma_m; \quad \gamma_{\theta\pm}^n = n_j(2\theta \pm i\gamma_j); \quad \omega_{ij} = \omega_{i0} - \omega_{j0} \end{aligned} \quad (3)$$

where indices  $i, j$ , and  $m$  number the sites;  $n = \{n_1, n_2, \dots, n_p, \dots, n_N\}$  is the set of integers describing the state of the phonon bath of the sites from  $j = 1$  to  $N$ ;  $n_j^\pm = \{n_1, n_2, \dots, (n_j \pm 1), \dots, n_N\}$ ;  $\theta = k_B T$ , where  $k_B$  is the Boltzmann constant and  $T$  is the temperature. The matrix elements of the auxiliary operators  $\sigma_{ii}^n$  and  $\sigma_{ij}^n$  at  $n = \{0, 0, \dots, 0\}$  are equal to the density matrix elements  $p_{ii}$  and  $p_{ij}$  corresponding to one-exciton populations and coherences in the site representation. Excitation of the  $j$ th site corresponds to  $\sigma_{ii}^n = 1$  for  $n = \{0, 0, \dots, 0\}$  and  $\sigma_{ii}^n = 0$  for other  $n$  sets. Subsequent phonon reorganization is described by evolution of the  $\sigma_{ii}^n$  elements with nonzero  $n$  values. Electronic energy transfers will be given by evolution of the coherences with other sites  $\sigma_{ij}^n$  and populations of these sites  $\sigma_{ii}^n$ . The hierarchically coupled equations are terminated if  $(n_1 + n_2 + \dots, n_N) > N_c$  as explained in refs 32 and 33. We use the  $N_c$  values from 7 to 12.

In eq 3, the excitonic mixing of the coupled sites is dependent on the phonon dynamics. For example, initial excitation of the Franck–Condon region of a few sites with a good overlap of the phonon wave functions may result in delocalization of the excitation. Further relaxation of the phonon modes to the bottom of individual potential surfaces may break the mixing of these sites, thus producing more localized excitations (so-called “dynamic localization”).

Equation 3 is derived for the high temperature limit, implying that  $\theta \gg \gamma_j$ .<sup>32,33</sup> Otherwise, low-temperature corrections should be applied.<sup>33</sup> In our case ( $\theta = 50 \text{ cm}^{-1}$  (77 K),  $\gamma_j = 35 \text{ cm}^{-1}$ ), eq 3 without applying a low-temperature correction can give two types of artifacts depending on the characteristic frequencies of the system under study. First, one can find negative site populations if the energy gap between the sites exceeds 150–200  $\text{cm}^{-1}$ . Second, if the sites are strongly coupled ( $M > 100 \text{ cm}^{-1}$ ), then the coherence between them can exceed their populations (thus giving negative exciton populations). Fortunately, the B800 antenna is characterized by equal site energies and small couplings ( $M = 20 \text{ cm}^{-1}$ ). For such a system, eq 3 is working without low-temperature corrections even at 77 K.

The linear spectra are determined by the first-order response to a weak optical field. In first order, the electric field creates a coherence  $p_{j0}$  between the ground and excited states of the molecule. The hierarchically coupled equations for the matrix elements corresponding to these coherences are

$$\begin{aligned} \dot{\sigma}_{j0}^n &= -[\gamma^n + i(\omega_{j0} - \omega)]\sigma_{j0}^n - i \sum_k M_{jk}\sigma_{k0}^n + i d_{j0}^e \sigma_{00}^n \\ &\quad + i\lambda_j \sigma_{j0}^{n_j+} + i\gamma_{\theta-}^n \sigma_{j0}^{n_j-} \end{aligned} \quad (4)$$

where  $d_{j0}^e$  is the projection of the transition dipole moment of the  $j$ th site  $\mathbf{d}_{j0}$  on the polarization vector of the electric field  $\mathbf{e}$ . In eq 4, we suppose that the amplitude of the electric field is time-independent and equal to unity. Initially, only the ground state is populated with  $\sigma_{00}^n = 1$  for  $n = \{0, 0, \dots, 0\}$  and  $\sigma_{00}^n = 0$  for other  $n$  sets, implying that the ground state phonons are equilibrated. The linear optical responses are determined by the

steady-state solution for  $\sigma_{j0}(n = \{00, \dots, 0\})$ , that is equal to the density matrix element  $p_{j0}$ .

The absorption spectrum  $OD(\omega)$  averaged over all possible orientations of the antenna complex with respect to the light polarization  $\mathbf{e}$  is given by

$$OD(\omega) = \frac{1}{3} \omega \operatorname{Im} \left\{ \sum_j \sum_\alpha d_{j0}^\alpha p_{j0}^\alpha(\omega) \right\} \quad (5)$$

where  $d_{j0}^\alpha$  denotes the  $x$ ,  $y$ , or  $z$  components of the dipole moment ( $\alpha = x, y$ , or  $z$ ) and where the  $x$ ,  $y$ , or  $z$  axes are connected with the pigment organization in the antenna complex. The term  $p_{j0}^\alpha$  means the steady-state solution of eq 4, where the  $d_{j0}^\alpha$  are replaced by  $d_{j0}^\alpha$ . Equation 5 is equivalent to the alternative representation of OD in the form

$$OD(\omega) = \frac{1}{3} \omega \operatorname{Im} \left\{ \sum_{i,j} \mathbf{d}_{j0} \mathbf{d}_{i0} p_{j0}^i(\omega) \right\} \quad (6)$$

where  $p_{j0}^i$  means the solution of eq 4 with  $d_{j0}^e = \delta_{ij}$ . The circular dichroism (CD) spectrum averaged over orientations is given by

$$CD(\omega) = \frac{2}{3} k_\omega \omega \operatorname{Im} \left\{ \sum_{i,j} [\mathbf{d}_{j0} \mathbf{d}_{i0}] (\mathbf{R}_j - \mathbf{R}_i) p_{j0}^i(\omega) \right\} \quad (7)$$

where  $k_\omega$  is the wavevector,  $\mathbf{R}_j$  is a radius-vector of the center of the  $j$ th transition dipole, and square brackets  $[\mathbf{d}_{j0} \mathbf{d}_{i0}]$  denote the vector product of the dipole moments.

The spectra (5–7) should be also averaged over realizations of the static disorder induced by slow conformational motion of the antenna. The static disorder is modeled by uncorrelated random shifts of the site energies taken from a Gaussian distribution with a fwhm of  $s = 140 \text{ cm}^{-1}$ . Notice that in our previous modeling of the B800 antenna of *Rs. molischianum*<sup>29</sup>  $s = 120 \text{ cm}^{-1}$  was used in order to fit the OD spectrum using the standard Redfield theory. Now we use a slightly larger value of  $140 \text{ cm}^{-1}$ , which allows a better fit with the HE and modified Redfield approaches (that give narrower homogeneous line shapes).

The spectra and excitation dynamics calculated with hierarchical equations (HE) are compared with the results obtained with other approaches, i.e., standard Redfield (SR), modified Redfield (MR), and standard (original) Förster theory (SF). The corresponding expressions for OD/CD spectra and equations for one-exciton dynamics are given in Appendices A and B. In all these approaches, we use the same spectral density and same parameters as in the modeling with HE.

In our numerical examples, we calculate the one-exciton dynamics with artificial initial conditions; i.e., we suppose that only one site is excited initially. The subsequent evolution can be directly obtained using the HE or SF theories that are dealing with the site representation. In contrast, the Redfield equation deals with the exciton representation, where the initial conditions should be given in terms of the exciton populations and coherences between the exciton states. Notice that in that case excitation of one site corresponds to the coherent excitation of many exciton states. Evolution of the exciton population and coherences is then given by a master equation with the Redfield relaxation tensor. Switching back to the site representation gives us the site populations/coherences that can be compared with the results of the HE and SF theories. In the modified Redfield equation, the initial conditions include

the exciton populations only. Thus, the situation with excitation of one site cannot be described correctly by the MR theory.

### 3. RESULTS

**3.1. Linear Spectra: Homogeneous B800 Ring.** First, we calculate the OD spectra for a homogeneous B800 ring of *Rs. molischianum* (eight B800 BChl's). In the absence of static disorder and without dynamic localization (as supposed in SR/MR), the excited state manifold consists of delocalized exciton eigenstates, i.e.,  $k = 0$ ,  $k = \pm 1$ ,  $k = \pm 2$ ,  $k = \pm 3$ , and  $k = 4$  levels shifted from the monomeric transition energy by  $2M$ ,  $M$ ,  $0$ ,  $-M$ , and  $-2M$ , respectively (see Figure 1, where the positions

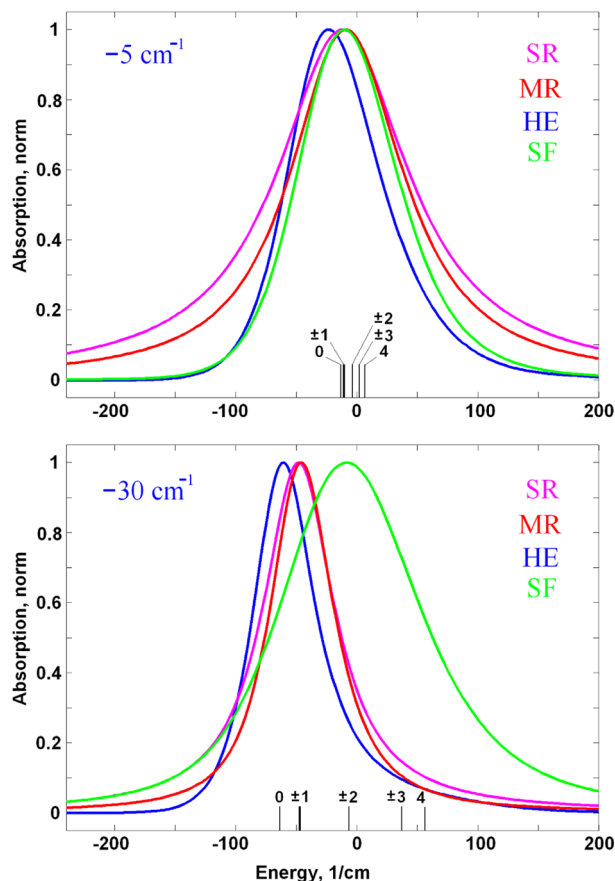


**Figure 1.** Comparing OD spectra for a homogeneous B800 ring ( $s = 0$ ) calculated with the standard Redfield (SR, magenta), modified Redfield (MR, red), hierarchical equations (HE, blue), and localized (Förster) model (SF, green). The spectra are calculated for two different pigment–pigment couplings, i.e.,  $M = -5 \text{ cm}^{-1}$  (top frame) and  $-30 \text{ cm}^{-1}$  (bottom frame) with  $\lambda = 25 \text{ cm}^{-1}$ ,  $\gamma = 35 \text{ cm}^{-1}$ , and  $T = 77 \text{ K}$ . The energy is counted from the energy of the pure electronic  $S_0 \rightarrow S_1$  transition (that is the same for all the sites). The vertical bars show the positions of the eight exciton levels ( $k = 0, \pm 1, \pm 2, \pm 3$ , and  $4$ ), including their reorganization shift. The dipole allowed  $k = \pm 1$  degenerate pair is shown by a thick bar (other levels shown by thin bars are forbidden). All the spectra are normalized to unity.

of these levels are shown including their reorganization shifts). For the in-plane orientation of the transition dipoles, all the dipole strength is concentrated in the two  $k = \pm 1$  levels broadened due to relaxation to other levels. This exciton relaxation between delocalized states (with a big spatial overlap of their wave functions) is rather fast, producing a significant

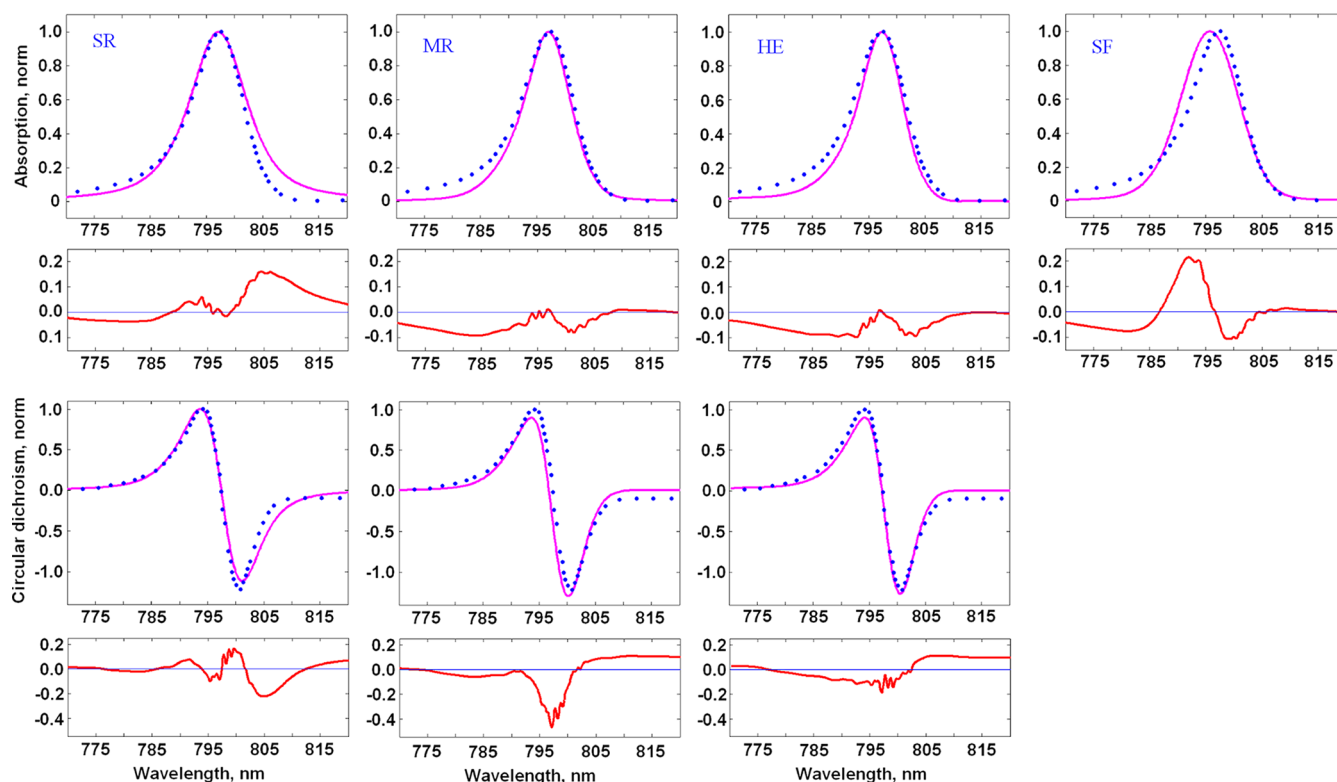


**Figure 2.** Fitting of the OD and CD spectra of the B800 band measured for *Rs. molischianum* at 77 K.<sup>31</sup> The measured spectra (blue points) are normalized to unity. Calculation (magenta lines) is done with the standard Redfield (SR), modified Redfield (MR), hierarchical equations (HE), and localized (Förster) model (SF). The Insets show the difference between the calculated and measured spectra (red lines). The calculated spectra are averaged over disorder ( $s = 140 \text{ cm}^{-1}$ ); the parameters are as follows:  $M = -20 \text{ cm}^{-1}$ ,  $\lambda = 25 \text{ cm}^{-1}$ ,  $\gamma = 35 \text{ cm}^{-1}$ . The CD is equal to zero in the SF model and therefore is not shown.

broadening. The largest broadening is observed for small couplings  $M$ , when all the levels are almost isoenergetic.

In our example, the SR/MR theories predict a too broad OD spectrum at  $M = -5 \text{ cm}^{-1}$  (as shown in Figure 1, top frame). The real spectrum is narrower, as shown by HE calculation. This narrowing is caused by dynamic localization destroying the exciton states and producing more localized excitations with slower hopping-type energy transfer. Notice that for  $M = -5 \text{ cm}^{-1}$  the HE approach almost coincides with the fully localized SF model. The only difference is the more asymmetric line shape predicted by HE.

Increase of coupling to  $M = -30 \text{ cm}^{-1}$  produces bigger splitting of the levels, thus blocking the uphill transfers from the  $k = \pm 1$  states. The allowed  $k = \pm 1$  levels become more red-shifted, more separated from higher levels, and not so broadened. The SR/MR models give the OD spectrum with a characteristic narrowing and red-shifting, in contrast to SF, where the exciton splitting is not included (see the lower frame of Figure 1, where the SF spectrum is peaking near the zero energy with some red-shifting due to reorganization). The HE spectrum is closer to the SR/MR picture, but the HE line shape is more asymmetric (Figure 1, bottom frame). We conclude that at  $M = -30 \text{ cm}^{-1}$  the exciton structure is not significantly destroyed by dynamic localization.

Notice that the narrowing upon  $M$  increase is not connected with the narrowing of the static disorder (which is absent in our example!) or narrowing of the phonon wing (in the Redfield picture, such narrowing is given by a product of the exciton wave functions (see eq A3), that are not dependent on  $M$  in the

homogeneous case). The only reason for the observed narrowing is the increased lifetime for the lower exciton states. In the absence of exciton effects (in the localized SF picture), we observe additional broadening of the OD at  $M = -30 \text{ cm}^{-1}$  instead of narrowing, because the transfer rate between the localized isoenergetic sites increases (in the Förster model) in proportion to  $M^2$ .

The results shown in Figure 1 are in agreement with the calculation of the B800 2D spectra at zero delay using modified Redfield theory. In particular, it has been shown that switching on the excitonic coupling results in a shift of the 2D spectrum along the diagonal to lower energy, homogeneous line narrowing, and appearance of the excited-state absorption band.<sup>26</sup> Obviously, the shift and narrowing of the 2D spectrum have the same origins as the shift and narrowing of the calculated OD spectra (Figure 1).

**3.2. Linear Spectra: Disordered Ring.** In order to reproduce the real spectra for the B800 band, we have to include the static disorder. The disorder results in a more uniform distribution of the dipole strength over the exciton states, the individual exciton states become more localized, and the splitting between them is increased. Spectral lines of individual exciton states become inhomogeneously broadened, whereas their homogeneous broadening increases in proportion to the participation ratio (that is bigger for localized states). Due to these line broadening effects, the difference between the spectral shapes obtained with the SR, MR, HE, and SF approaches is not so pronounced but is still sizable, giving rise to some specific features (Figure 2).



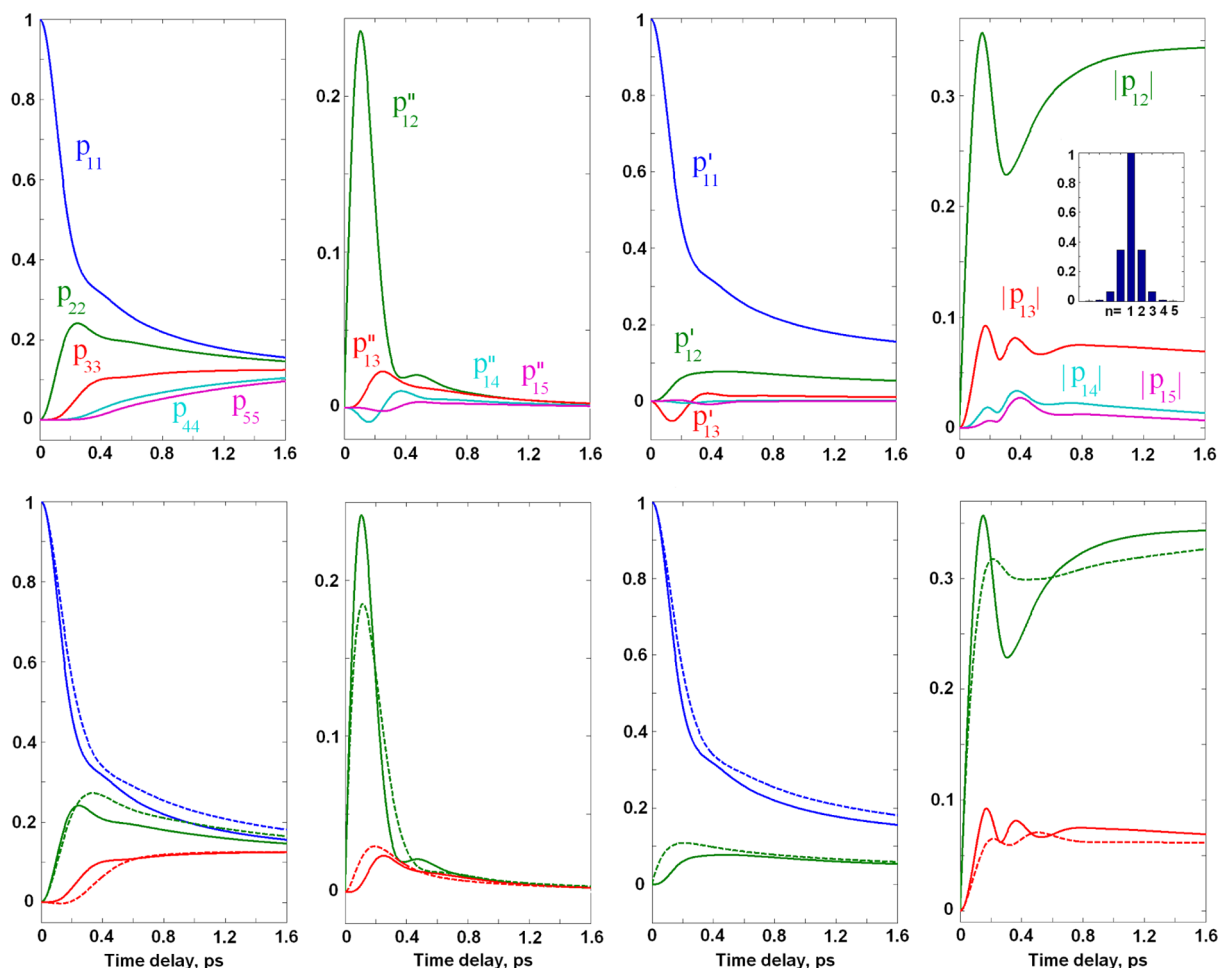


**Figure 3.** Excitation dynamics of the homogeneous ( $s = 0$ ) B800 ring at 77 K with artificial initial conditions ( $n = 1$  site is initially populated). Parameters are the same as in the fit of the spectra (Figure 2). Top frames: Dynamics of the site populations  $p_{nn}$ , imaginary ( $p''_{1n}$ ) and real part ( $p'_{1n}$ ) of the coherences  $p_{1n}$  (where  $n = 2, 3, 4, 5$ ), and absolute values of the coherences  $p_{1n}$  normalized to  $p_{11}$  (denoted as  $|p_{1n}|$ ). The inset shows the distribution of the steady-state values of  $|p_{1n}|$  (calculated at 5 ps delay) as a function of  $n$ . Calculation is done with the HE method. Bottom frames: The same dynamics as in the top but calculated with the HE (solid lines) and SR (dashed lines) approaches.

The SR model (implying weak exciton–phonon coupling) gives a symmetric Lorentzian line shape for each exciton level. The resulting OD/CD spectra are almost symmetric and display broad Lorentzian wings. Due to this wing, the red tails of the measured OD and CD are not well reproduced.

The MR model yields asymmetric line shapes (due to strong exciton–phonon coupling) with a better fit of the red wing. The line shape can be even more asymmetric (i.e., with better fit of the blue wing of the OD) if we include high-frequency modes in the exciton–phonon spectral density (data not shown).

The HE approach gives spectra that are very similar to those predicted by MR but slightly narrower. Again, the blue wing of the OD is not reproduced because we are restricted to a low-frequency spectral density. However, in contrast to MR, in the HE method, one cannot extend the calculation to an arbitrary spectral density. Inclusion of just one additional vibrational mode will greatly increase the number of hierarchically coupled equations.

Finally, the localized SF model predicts more symmetric line shapes that are determined by the sum of contributions from noninteracting sites. Notice, in this respect, that the OD asymmetry is generally determined by two factors: (i) the

disordered exciton structure of the ring, with intense red states and weakly allowed higher states producing the broad blue wing, and (ii) the phonon-induced asymmetry of each exciton (or localized) state. In the MR and HE models, both factors contribute to the OD line shape, whereas in the SF model only the second factor is included. Comparing asymmetric MR/HE profiles with the symmetric SF spectrum, we conclude that the experimentally observed asymmetry of the OD is largely determined by excitonic effects. Such a kind of exciton-induced asymmetry in the B800 OD was discussed by Cheng and Silbey.<sup>30</sup> The same asymmetry should also be present in the SR spectrum, but there it is masked by the large homogeneous broadening.

**3.3. Excited-State Dynamics in the Homogeneous B800 Ring: HE vs Redfield Picture.** Using the parameters obtained from the fit of the spectra (Figure 2), we can now model the excited-state dynamics. First we perform this for a homogeneous ring with artificial initial conditions (supposing that the site  $n = 1$  is initially populated, whereas all other initial populations and coherences are set to zero). Using the HE method, we calculate the dynamics of the one-exciton density matrix in the site representation. In Figure 3, we show populations  $p_{nn}$  and coherences  $p_{1n}$  for half of the ring ( $n = 1$ –

5) (due to symmetry, the  $p_{nm}$  and  $p_{1n}$  values with  $n = 6, 7$ , and  $8$  are the same as those with  $n = 4, 3$ , and  $2$ , respectively). Initial excitation of one site is followed by transfer of populations to other sites together with formation of the coherences between the sites (generated from the site populations due to pigment–pigment couplings  $M_{ij}$ ).

Notice that the imaginary parts of the coherences in the site representation  $p''_{1n}$  are responsible for creation of the coherences between the exciton states. If they are oscillating, they will produce beats in the third-order spectral responses (pump–probe anisotropy, 2D photon echo). If they exhibit aperiodic decay, they will give non-oscillatory contributions to spectral responses, for example, additional anisotropy decaying with the same time scale.

The real parts of the coherences  $p'_{1n}$  are responsible for the delocalization of the exciton states. In contrast to  $p''_{1n}$ , the real parts  $p'_{1n}$  do not decay to zero but reach some steady-state value, that determines the delocalization of the steady-state exciton wavepacket. This wavepacket reflects a superposition of the exciton states populated at thermal equilibrium. Typically, the wavepacket is more localized than individual exciton states (depending on how many states are populated and superimposed). The degree of delocalization of the exciton wavepacket is usually characterized by the so-called “coherence length”, defined as an effective width of the antidiagonal distribution of the density matrix  $p_{nm}$  in the site representation.<sup>43–45</sup> This distribution can be viewed as a plot of the absolute values of  $p_{1n}$  as a function of  $n$  (including the diagonal value  $p_{11}$ ). The width (fwhm) of this distribution can be defined as an exciton (coherence) length,  $N_{\text{coh}}$ . The steady-state value of  $N_{\text{coh}}$  (shown in the inset of Figure 3) is determined by the steady-state values of the real parts  $p'_{1n}$  (because imaginary parts decay to zero). In our example,  $N_{\text{coh}} = 1.53$ , according to the HE model. To visualize the coherence length as a function of time, it is convenient to use the absolute values of  $p_{1n}$  normalized to  $p_{11}$  at every time delay (see the right frame in Figure 3). Notice that initial excitation is supposed to be completely localized at the site  $n = 1$ . This is followed by a quick delocalization with a formation of the exciton wavepacket (with the delocalization length  $N_{\text{coh}}$ ) during about 0.2 ps. This quick delocalization determines a fast phase of the population kinetics (see fast equilibration of the  $p_{11}$  and  $p_{22}$  populations during 0.2 ps). This phase is then followed by a motion of the exciton wavepacket around the ring with slow equilibration of all the populations. In the homogeneous case shown in Figure 3, this equilibration occurs with the time scale of about 1.5–2 ps.

In Figure 3, we also compare the dynamics calculated with the HE and SR approaches. The Redfield picture gives populations and coherences that are close to those obtained with the HE. On the sub-ps time scale, both models display an oscillatory coherent behavior, but HE predicts larger oscillatory amplitudes. The lifetime of the biggest coherence  $p''_{12}$  is about 0.4 ps in the HE and SR, determined by our choice of the spectral density. The slow (noncoherent) equilibration is very similar in both models, but the SR gives a bit slower dynamics. In the steady-state limit, the SR theory predicts almost the same value of delocalization  $N_{\text{coh}}$  as the HE. This implies that the phonon-induced (dynamic) localization is negligible in our case, so that the localization is mostly determined by the thermal mixing of the exciton wave functions (remember we consider a homogeneous ring here). For the disordered ring,

there must be additional localization by the static disorder (see below).

**3.4. Excited-State Dynamics in a Homogeneous LH2 Ring Consisting of Eight B800 BChl's: Secular vs Nonsecular Redfield.** In this section, we continue to explore the excitation dynamics in a homogeneous ring of eight B800 BChl's. In order to gain a deeper insight into the interplay of the populations and coherences, it is useful to compare the full (nonsecular) and secular version of the SR theory (with the full and secular  $R_{kk'pp'}$  tensor in eq A1). Below we denote these two versions as  $\text{SR}_f$  and  $\text{SR}_s$ , respectively. The relation between them is strongly dependent on the pigment–pigment coupling value  $M$ .

For strong coupling ( $-60 \text{ cm}^{-1}$ ), the difference between the three theories is not so big. The full Redfield  $\text{SR}_f$  gives the same oscillatory amplitudes as the HE model, but oscillations exhibit faster decay. In the secular Redfield  $\text{SR}_s$ , the oscillations decay even faster and also the oscillatory amplitudes are significantly reduced. Interestingly, the  $\text{SR}_s$  predicts the same oscillatory period as HE, whereas this period is larger in the  $\text{SR}_f$  picture (see discussion below).

Decrease of coupling to  $-40$  and  $-30 \text{ cm}^{-1}$  results in more pronounced differences between the secular  $\text{SR}_s$  and nonsecular approaches ( $\text{SR}_f$  and HE). The amplitude of the first maximum of the coherence  $p''_{12}$  developing during 50 fs is significantly less in  $\text{SR}_s$ . Also, the population  $p_{11}$  decay becomes faster in the secular version displaying an increasingly larger deviation from both  $\text{SR}_f$  and HE.

In the weak coupling case ( $-20, -12$ , and  $-7 \text{ cm}^{-1}$ ), the initial population decay occurs in the ps time scale. Nonsecular theories predict also a very long-lived coherence. In contrast, the coherence in the secular case decays quickly (i.e., during 0.25 ps). Population equilibration in the  $\text{SR}_s$  picture is unrealistically fast, showing an about 100 fs time constant.

On the other hand, for a very weak coupling ( $-12$  and  $-7 \text{ cm}^{-1}$ ), some deviation exists of the full Redfield from the HE. According to the  $\text{SR}_f$  model, the amplitude of the coherence  $p''_{12}$  developing in 100–200 fs is significantly smaller than that for the HE approach. Besides, the population  $p_{11}$  decay is slower compared to HE.

Comparing the difference between the secular and nonsecular kinetics in the examples above, we conclude that nonsecular terms (coupling between one-exciton populations and coherences between the exciton states) give only a minor contribution to the dynamics in the case of strong exciton coupling but can change dramatically the apparent kinetics in the weakly coupled antenna.

The strongly coupled system is characterized by a big exciton splitting, so that the coherences between exciton states  $p_{k_1k_2}$  are oscillating at high frequencies  $\omega_{k_1k_2}$  that are very different for different pairs of the eigenstates ( $k_1, k_2$ ). Thus, the coherence to coherence ( $p_{k_1k_2} \leftrightarrow p_{k_3k_4}$ ) and population to coherence transfers ( $p_{k_1k_2} \leftrightarrow p_{k_1k_1}, p_{k_2k_2}$ ) are essentially nonresonant, and therefore not effective (at least on the time scale exceeding  $(\omega_{k_1k_2} - \omega_{k_3k_4})^{-1}$  or  $(\omega_{k_1k_2})^{-1}$ , respectively).

In the case of weak coupling, the splitting  $\omega_{k_1k_2}$  is small and there is no significant difference between the pure population ( $p_{k_1k_1} \leftrightarrow p_{k_2k_2}$ ) and population to coherence transfers ( $p_{k_1k_2} \leftrightarrow p_{k_2k_2}, p_{k_1k_1}$ ) even on the ps time scale. The coherences are continuously repumped from the populations, and the density matrix determined by a coherent superposition of  $p_{k_1k_1}, p_{k_2k_2}$ , and  $p_{k_1k_2}$  remains localized in the site representation. In other words, in the presence of coherences, the excitations keep

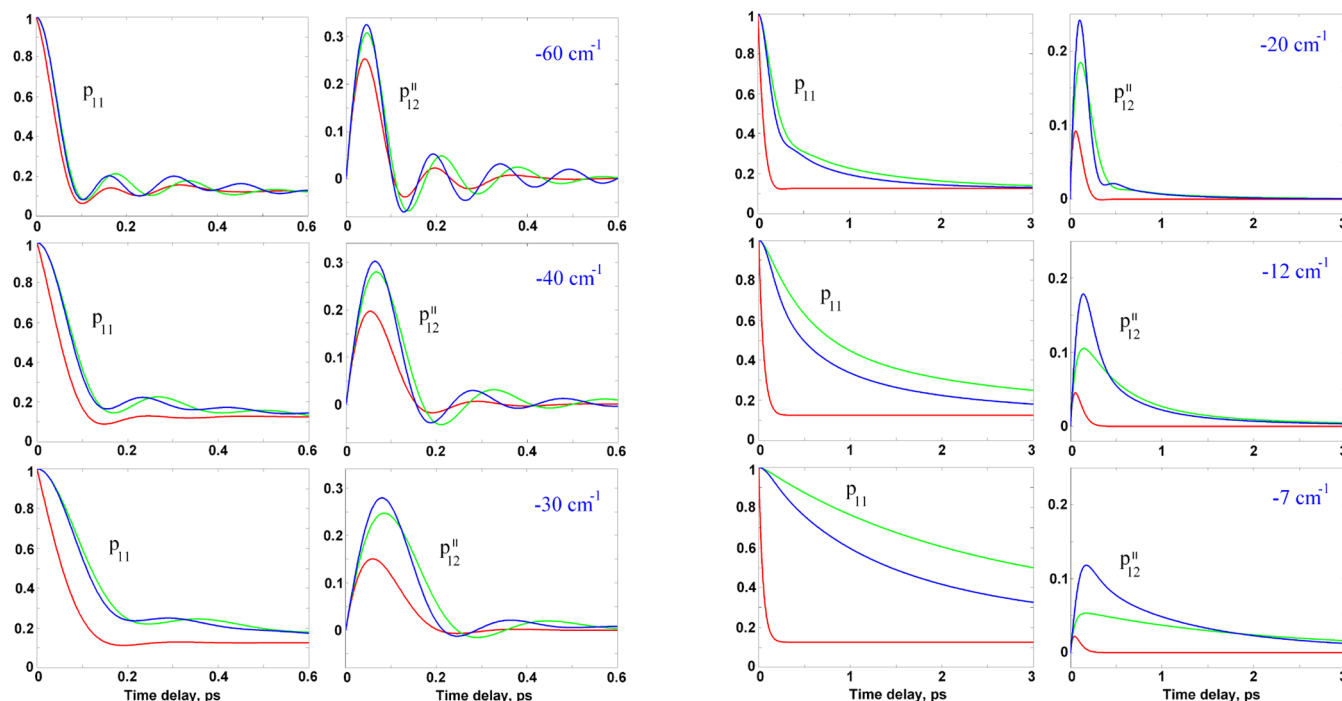


**Figure 4.** Excitation dynamics in a homogeneous LH2 ring consisting of eight B800 BChl's with initial population of the site  $n = 1$  at  $T = 77$  K. Parameters are the same as in previous examples (Figures 2 and 3), but the pigment–pigment couplings are different, i.e.,  $M = -60, -40, -30, -20, -12$ , and  $-7$   $\text{cm}^{-1}$ , as indicated on the frames. For each coupling value, we calculate the population of the initially excited site  $p_{11}$  and imaginary part of the coherence  $p_{12}''$  using the HE (blue),  $\text{SR}_f$  (green), and  $\text{SR}_s$  (red) theories. Note the different time scales for strong and weak couplings, i.e., 0.6 ps ( $M = -60, -40$ , and  $-30$   $\text{cm}^{-1}$ ) and 3 ps ( $M = -20, -12$ , and  $-7$   $\text{cm}^{-1}$ ).

memory about their initial localization, and this can significantly slow down the transfer to other sites. Without repumping from the populations (as supposed in the  $\text{SR}_s$  model), the coherences decay very quickly (in 100–200 fs for all couplings, as shown in Figure 4), rapidly resulting in the formation of a density matrix determined by the noncoherent contribution from delocalized exciton eigenstates. The relaxation between exciton states is very fast (about 100 fs in our examples) and does not depend on the exciton coupling  $M$  (because an overlap of the exciton wave functions does not depend on  $M$  in the homogeneous case). Thus, we obtain the 100 fs equilibration even in a very weakly coupled systems (see the  $\text{SR}_s$  kinetics at  $M = -12$  and  $-7$   $\text{cm}^{-1}$ ), whereas more realistic approaches ( $\text{SR}_f$  and HE) give time constants of several ps in the case of (very) weak coupling.

Similar unrealistically fast transfers have been obtained with the modified Redfield (MR) theory, where the coherences are not included at all.<sup>46</sup> Considering two weakly coupled isoenergetic sites, we formally obtain a delocalization between them. The MR theory (where the coherences between exciton states are neglected) gives a sub-100 fs population transfer in such systems for  $M < 15$ – $20$   $\text{cm}^{-1}$ . To exclude this “resonant artifact”, a combined Förster–Redfield theory can be used, where the transfers between weakly coupled sites ( $M < M_{\text{cr}} = 15$ – $20$   $\text{cm}^{-1}$ ) and relaxation within strongly coupled clusters (with  $M > M_{\text{cr}}$ ) are described by the generalized Förster and modified Redfield theories, respectively.<sup>46–49</sup> As nicely shown in Figure 4, this fast artifact is absent in the  $\text{SR}_f$  approach and in the more general HE approach.

Although the nonsecular  $\text{SR}_f$  and HE theories predict similar kinetics, it can be concluded that they give a slightly different treatment of the nonsecular interplay between the populations and the coherences. In particular, the  $\text{SR}_f$  model displays a

slower aperiodic decay of the population and the coherences in the weak coupling case ( $M = -12$  and  $-7$   $\text{cm}^{-1}$ ). On the other hand, the oscillatory kinetics in the strong coupling case exhibit larger oscillatory periods in the  $\text{SR}_f$  model compared to HE. Switching off the nonsecular terms (in the  $\text{SR}_s$  model) results in the same oscillatory period as in HE. The origin of this difference is not completely clear. However, one can suppose that probably the population-to-coherence transfers are slower in  $\text{SR}_f$  due to the one-phonon character of relaxation in the standard Redfield (see also the discussion of this issue in the next section).

**3.5. Equilibration in a Disordered B800 Ring.** Now we wish to study the effect of site inhomogeneity on the excited state kinetics. As a first example, we consider the homogeneous ring with just one site shifted in energy. Three top frames in Figure 5 show the same kinetics as in Figure 4 but with the initially excited site ( $n = 1$ ) shifted to the blue. When the shift exceeds the characteristic frequency of the spectral density ( $\gamma = 35$   $\text{cm}^{-1}$ ), the kinetics become slower. This slowdown is not so big in the HE picture, but it is really huge in the  $\text{SR}_f$  and  $\text{SR}_s$  models. The standard Redfield implying a weak exciton–phonon coupling describes relaxation between eigenstates as a one-phonon process. If the donor–acceptor energy gap is bigger than the phonon frequency, the transfer rates become too slow in contrast to multiphonon theories (modified Redfield and Förster), as was first pointed out by Yang and Fleming.<sup>50</sup> Notice that both  $\text{SR}_f$  and  $\text{SR}_s$  rates are decreased. Our example shows that not only population but also nonsecular population–coherence transfers are slowed down, decreasing both the amplitude and decay rate of the coherence  $p_{12}''$  in the  $\text{SR}_f$  model. Thus, the difference between secular and nonsecular coherences  $p_{12}''$  is reduced as well as the difference



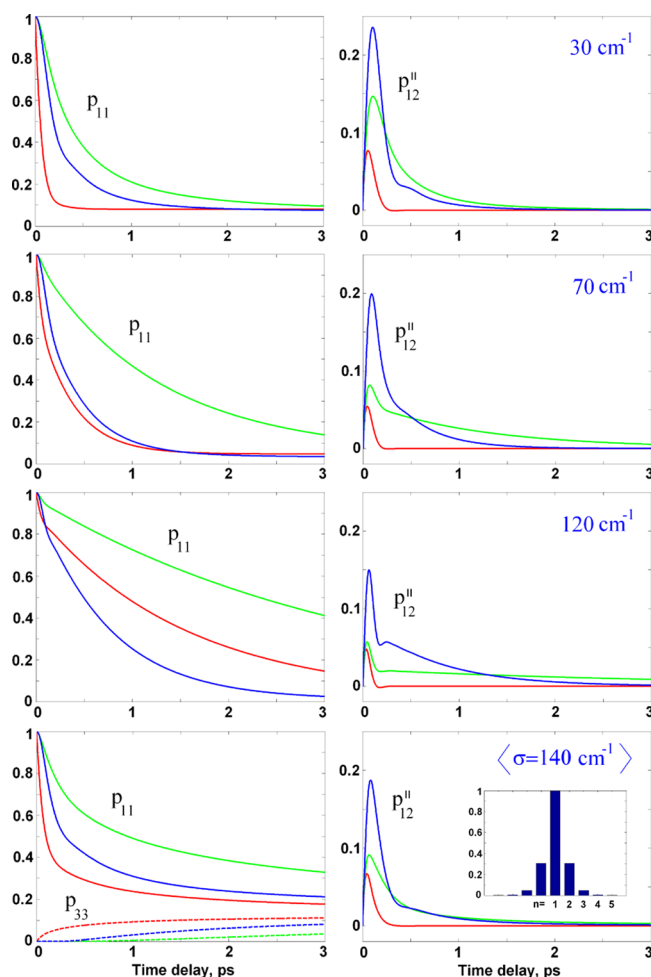


**Figure 5.** Excitation dynamics in a disordered LH2 ring consisting of eight B800 BChl's with initial population of the site  $n = 1$ . Spectral density is the same as in previous examples (Figures 2–4); the pigment–pigment coupling is  $M = -20 \text{ cm}^{-1}$ ,  $T = 77 \text{ K}$ . We calculate the population of the initially excited site  $p_{11}$  and imaginary part of the coherence  $p_{12}''$  using the HE (blue),  $\text{SR}_f$  (green), and  $\text{SR}_s$  (red) theories. The three top frames show the simplest model for the site inhomogeneity, where only one site (i.e., the initially excited site  $n = 1$ ) is blue-shifted by 30, 70, and  $120 \text{ cm}^{-1}$  (as indicated in the frames). In the bottom frame, all the sites exhibit random shifts of the transition energies modeled by uncorrelated Gaussian disorder with a fwhm of  $s = 140 \text{ cm}^{-1}$ . The calculated kinetics are averaged over disorder. The population of the initially excited site  $p_{11}$  (solid lines) is shown together with the population  $p_{33}$  of the  $n = 3$  site (dashed lines). The inset shows the antidiagonal decay of the density matrix, i.e., the distribution of the steady-state values of  $|p_{1n}|$  as a function of  $n$  (as obtained for the HE model at 15 ps delay).

between the  $\text{SR}_f$  and  $\text{SR}_s$  populations (compare the difference in  $p_{11}$  kinetics in the 30 and  $120 \text{ cm}^{-1}$  cases in Figure 5).

Finally, we calculated the kinetics averaged over Gaussian disorder of all the sites (bottom frame in Figure 5). The fast (0.2 ps) phase of the  $p_{11}$  decay is determined by quick delocalization of the initially localized excitation (yielding equilibration of the  $p_{11}$  and  $p_{22}$  populations). This phase is followed by a slow (several ps) motion of the exciton wavepacket around the ring. Comparing the  $p_{11}$  and  $p_{33}$  kinetics (Figure 5, bottom), we see that population equilibration is really slow in the disordered ring. In the homogeneous case, all the populations  $p_{11}$ – $p_{55}$  almost reach equilibrium already in 1.5–2 ps (see Figure 3). However, in the

presence of the disorder, the  $p_{33}$  population grows with a time constant of about 3–4 ps in the HE picture. The averaged  $\text{SR}_f$  and  $\text{SR}_s$  kinetics are closer to the HE model than in single realizations, but the averaged  $\text{SR}_f$  dynamics is still too slow, whereas the  $\text{SR}_s$  one is too fast.

A steady-state wavepacket exciton formed at equilibrium has a coherence length of  $N_{\text{coh}} = 1.43$ , which is only slightly less than the homogeneous value  $N_{\text{coh}} = 1.53$  determined by thermal-induced localization. The degree of delocalization is generally determined by the smallest of the disorder-induced length, thermal-induced length, phonon-induced length (dynamic localization), and polaron-induced length.<sup>43,51</sup> In the case of B800, both the disorder and the thermal lengths are small, producing localization with  $N_{\text{coh}} < 2$ , i.e., predominant localization at one site with some coherence with the neighbors. The phonon length is larger, as can be concluded from the negligible difference between the  $N_{\text{coh}}$  in the HE and  $\text{SR}$  models (as discussed above). Polaron effects are not accounted for in our models (including HE), but bearing in mind the good explanation of the excitonic OD/CD spectra (as shown in Figure 2), we can safely assume that the polaron length is also relatively large in the B800 antenna.

### 3.6. Population Dynamics: Redfield vs Förster Picture.

In this section, we compare the results obtained for a homogeneous ring using the Redfield and Förster theories. As a trial, we use the HE model. Figure 6 shows the site population dynamics calculated for different coupling values varying from the very weak ( $-7 \text{ cm}^{-1}$ ) to the strong coupling limit ( $-75 \text{ cm}^{-1}$ ).

In the weak coupling limit ( $-7$  and  $-15 \text{ cm}^{-1}$ ), the  $\text{SR}_f$  gives slower equilibration than HE (this we have seen already in Figure 4). It can be demonstrated that this feature is not connected with the dynamic localization. Calculation of the time-dependent coherence length shows that the HE model does not predict any additional phonon-induced localization (data not shown). In contrast, the  $\text{SR}_f$  gives a bit more localized wavepacket (responsible for slower dynamics) at earlier delays (i.e.,  $< 5 \text{ ps}$  and  $< 2 \text{ ps}$  for  $M = -7$  and  $-15 \text{ cm}^{-1}$ , respectively). The origin of this phenomenon cannot be directly assigned, but it is clear that this is a result of some complicated interplay of population and coherences. On the other hand, the Förster model works much better in the weak coupling limit ( $-7$  and  $-15 \text{ cm}^{-1}$ ), as shown in the bottom frames of Figure 6. It is remarkable that for these couplings the fully localized SF model gives quantitatively the same population kinetics as the HE (that in this case predicts some delocalization and sizable coherences).

In the strong coupling case, the population kinetics display oscillations, that are reproduced by the  $\text{SR}_f$ , whereas SF theory does not include oscillations at all but nicely reproduces the non-oscillatory part of the kinetics. If we visualize energy transfer in the site representation as a motion of a delocalized wavepacket, then we can say that the SF model correctly describes the motion of its center while neglecting the coherences that determine the shape of the wavepacket wings. Obviously, the features of the spectral responses determined by these coherences (off-diagonal kinetics of the 2D echoes, pump–probe anisotropy, etc.) can never be explained by the SF model. For example, the fast (sub-ps) anisotropy decay in the B800 antenna<sup>14</sup> was not possible to fit with the SF. However, switching to the  $\text{SR}_f$  picture allowed a quantitative fit of the fast (sub-ps) and slow ( $> 3 \text{ ps}$ )



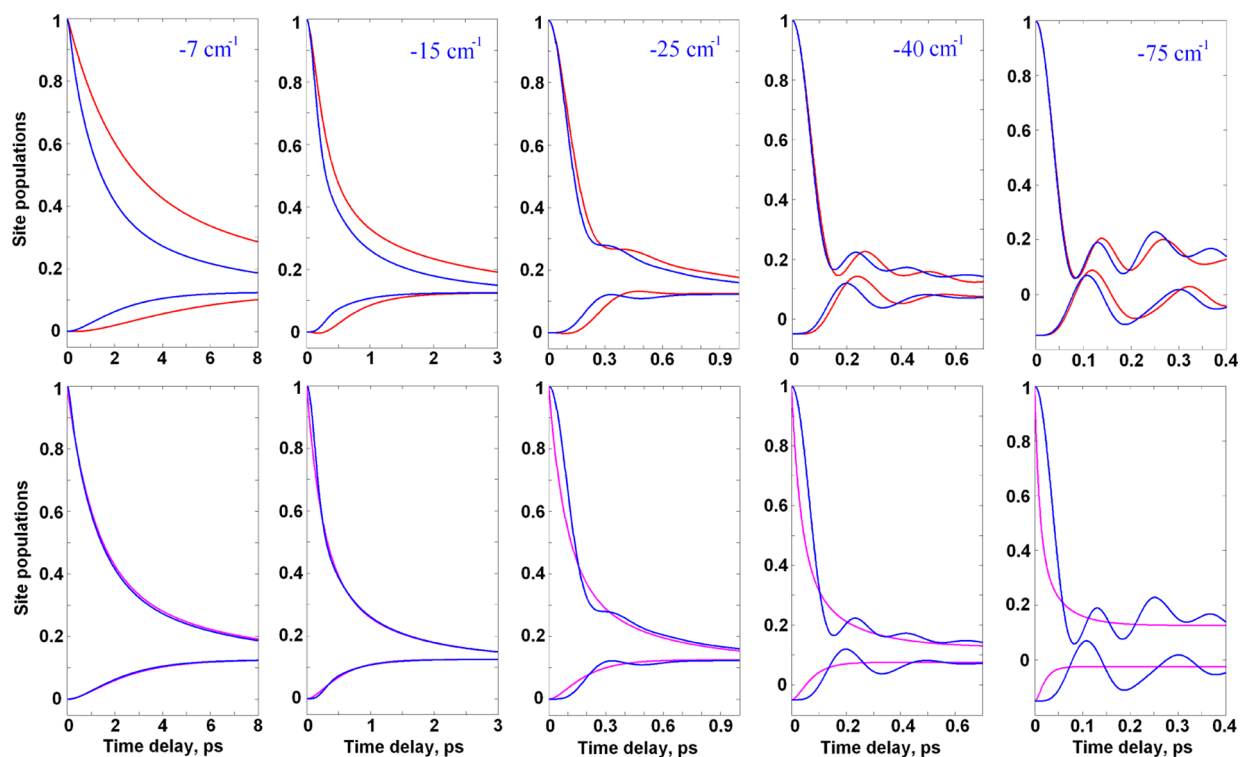


**Figure 6.** Excitation dynamics in a homogeneous ring (with initial population of the site  $n = 1$ ) calculated with the Redfield and Förster theories at  $T = 77$  K. Only  $p_{11}$  and  $p_{33}$  populations are shown ( $p_{33}$  corresponds to the lower curves starting from zero). The spectral density is the same as in previous examples (Figures 2–5), and the pigment–pigment couplings are different, i.e.,  $M = -7, -15, -25, -40$ , and  $-75$   $\text{cm}^{-1}$ , as indicated on the frames. Note the different time scales used for different  $M$  values, 8, 3, 1, 0.7, and 0.5 ps. The  $p_{33}$  kinetics in the 40 and 75  $\text{cm}^{-1}$  frames are shifted down by 0.05 and 0.15 to avoid overlap with the  $p_{11}$  trace. Top frames: population kinetics calculated using the HE (blue) and  $\text{SR}_f$  (red). Bottom frames: population kinetics calculated using the HE (blue) and SF (magenta).

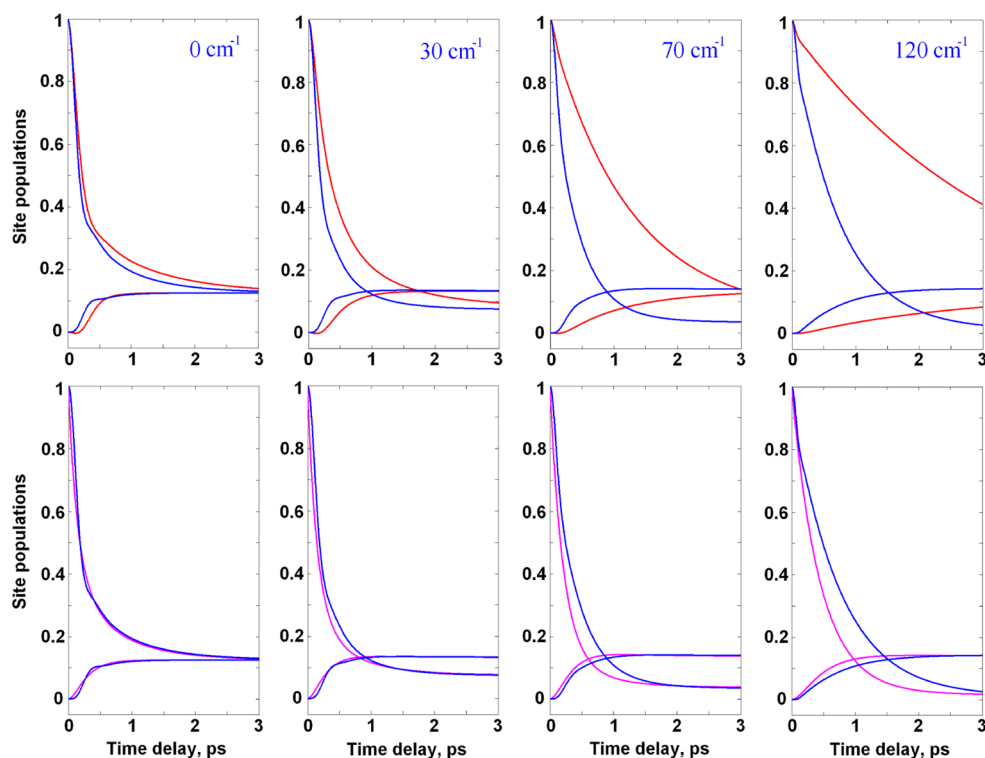


**Figure 7.** The same as in Figure 6, but instead of a homogeneous ring, we consider the case when one site (i.e., initially excited site  $n = 1$ ) is blue-shifted by 30, 70, and 120  $\text{cm}^{-1}$  (as indicated on the frames). The zero shift (left frame) corresponds to the homogeneous case. The pigment–pigment coupling is fixed to  $M = -20$   $\text{cm}^{-1}$ .

Table 1. Comparison of Different Theoretical Approaches to the Energy Transfer Dynamics<sup>a</sup>

	big energy gap	coherence between sites	coherence between exciton states	population–coherence transfers	weakly coupled isoenergetic sites	realistic line shape/spectral density	dynamic localization	polaron effects
SR <sub>s</sub>	–	+	+	–	–	–/+	–	–
SR <sub>f</sub>	–	+	+	+	+	–/+	–	–
MR	+	+	–	–	–	+/+	–	–
SF	+	–	–	–	+	+/+	–	–
HE	+	+	+	+	+	+/-	+	–

<sup>a</sup>In the eight columns, we list eight specific features included (+) or not included (–) in the theories. The comments about each feature are in the text (see points 1–8 in the Discussion section).

depolarization, determined by the coherence decay and energy migration around the ring, respectively.<sup>29</sup>

Figure 7 shows the same kinetics as in the previous example, but now we consider the homogeneous ring with one site shifted in energy; i.e., the initially excited site ( $n = 1$ ) is shifted to the blue. As we have seen in previous examples (see Figure 5), the SR<sub>f</sub> theory gives too slow kinetics when the energy gap between the  $n = 1$  and other sites starts to exceed the characteristic phonon frequency ( $\gamma = 35 \text{ cm}^{-1}$ ). Comparing it to the SF theory (Figure 7), we conclude that the Förster picture is quantitatively more correct (because the Förster model does not imply a weak phonon coupling, thus including multiphonon transfers). On the other hand, the Förster picture does not include coherences that can contribute to the population equilibration via nonsecular transfers. This may cause some discrepancy between the SF and HE models. The most sizable deviation of the SF kinetics from the HE model appears in the case of big energy gaps (see the  $120 \text{ cm}^{-1}$  frame), but this deviation is still much smaller than in the SR<sub>f</sub> picture.

#### 4. DISCUSSION

The analysis performed in the present study illustrates the specific features of different theoretical approaches. Kinetics calculated for the B800 antenna show the limitations of perturbative approaches as compared to the exact (non-perturbative) solution given by the hierarchical equation method. In the examples shown above, we demonstrate that these limitations can change the character of the kinetics (oscillatory vs aperiodic decay) and the corresponding time scales (up to 1–2 orders). The advantages and shortcomings of different approaches are summarized in Table 1. Most of them are well understood in general, but it is important to know how they manifest themselves at a quantitative level in a concrete (real) system. In this paper, we show this for the B800 antenna of LH2, for which the coupling values are near the boundary between the strong and weak coupling limit.

(1) The SR theories imply weak exciton–phonon coupling, where only single quantum transitions of the phonon state are allowed.<sup>50</sup> Thus, the energy gap of the two exciton states must be exactly matched by the frequency of a phonon mode. For instance, for the spectral density in a form of eq 2, the transfer rate will be strongly underestimated if the gap between the two exciton states exceeds the characteristic phonon frequency  $\gamma$ . In contrast, this is not the case in the models with strong exciton–phonon coupling, i.e., HE, SF, and MR (as indicated in the first column in Table 1). In our model of B800, the phonon frequency ( $\gamma = 35 \text{ cm}^{-1}$ ) is significantly less than the disorder value ( $s = 140 \text{ cm}^{-1}$ ). As a result, the rates obtained with the SR models can be several times less than those obtained with the

models with strong exciton–phonon coupling (HE, SF) for a significant fraction of the realizations. In order to obtain more relevant kinetics, the SR model for B800 can be generalized by including high-frequency terms in the spectral density as we did in ref 29.

(2) The exciton couplings between the sites (responsible for formation of the exciton states) are included explicitly in all the models except SF (see second column in Table 1). In the SF picture, the excitations are supposed to be localized, and transfers between them are described by taking the couplings as perturbations. For B800, the SF gives reasonably good kinetics for the site populations but fails to explain the linear spectra (containing excitonic features) and coherent components in the nonlinear kinetics.

(3) Broad-band excitation can create a coherent superposition of the exciton states. Dynamics of these coherences is included in the SR and HE, giving rise to oscillations in the nonlinear responses for strongly coupled clusters or to additional components with aperiodic decay for weakly coupled complexes. The lifetimes of the coherent oscillations (or the amplitude of the coherent peak in the aperiodic case) are larger in the HE approach, whereas, in the SR model, which implies infinitely fast phonon relaxation, the coherent features are reduced (see discussion of this issue in ref 32). In the case of the B800 antenna, the HE coherences are about 2 times bigger than predicted by the SR<sub>f</sub> model (see kinetics averaged over disorder in Figure 5). These coherences exhibit an almost non-oscillatory decay with characteristic times of 0.4–0.5 ps (70% amplitude) and 1–1.5 ps (30%). Such decoherence dynamics determines the fast TA anisotropy decay (not connected with any population transfer).<sup>14,29</sup>

(4) The coherent features (lifetime and amplitude of the first peak) are significantly different for the full (SR<sub>f</sub>) and secular (SR<sub>s</sub>) versions of the Redfield theory. Neglecting the population-to-coherence transfers (in the SR<sub>s</sub>) results in much faster coherence decay. In the full version (SR<sub>f</sub>), the coherences can be maintained for a very long time due to continuous repumping from the exciton populations. The results obtained with the SR<sub>f</sub> are close to the HE picture, where all the relaxation channels are included explicitly (see Figure 4). Notice that the nonsecular population-to-coherence transfers are more pronounced in the case of weakly coupled systems characterized by small splitting between the exciton states. In this case, the coherences between pairs of exciton states are varying slowly in time, and, therefore, better connected with the non-oscillating populations (in contrast to the fast oscillating coherences in the strongly coupled clusters). In the very weak coupling limit (when the coherences are almost in phase with the populations), an effective repumping from the populations can preserve long-lived (up to several ps) coherences.

(5) Energy transfer between weakly coupled sites is well described by the site-representation theories, i.e., HE and SF. For a very weak coupling, they give exactly the same results. In the exciton-representation approaches (SR<sub>s</sub>, SR<sub>p</sub>, MR), the dynamics within weakly coupled and isoenergetic sites can be correctly reproduced only if nonsecular terms are included (i.e., only in the SR<sub>f</sub> version). In the Redfield (eigenstate) picture, the localization is described by a coherent superposition of the delocalized exciton states and the coherences between them. Neglecting the coherences makes excitations delocalized, producing ultrafast equilibration even in the very weak coupling limit. Thus, in the MR picture, time constants of less than 100 fs can be formally obtained at  $M \rightarrow 0$ .<sup>46</sup> A similar behavior occurs in the SR<sub>s</sub> picture, where the coherences decay quickly in the absence of nonsecular transfers (see examples in Figure 4). In contrast, in the full SR<sub>f</sub> version, the localization can be maintained for a long time due to the presence of long-lived coherences. This gives a more realistic picture of energy transfer that is close to the localized SF picture.

(6) In the SR, the relaxation rates are calculated using an arbitrary spectral density, but the dephasing (that determines the line shapes) is described by a simple exponential decay, thus giving symmetric (Lorentzian) line shapes. In the MR and SF, the dephasing is determined by the line-broadening functions  $g(t)$  (eqs A5 and A9), giving more realistic asymmetric line shapes with vibrational wings. The nonperturbative HE approach is expected to give the most realistic line shape. For our B800 model, the HE line shape is very similar to the MR case but is more asymmetric (see Figure 1). Remember that in the MR only diagonal (in the exciton basis) coupling to phonons is included explicitly, whereas the off-diagonal part of coupling is taken into account perturbatively. In the HE, all the phonons are included nonperturbatively, thus giving a different (more realistic) line shape.

Unfortunately, in the HE method, it is difficult to switch from a simple spectral density (in the form of an overdamped Brownian oscillator or a single underdamped vibration) to a more realistic density containing up to several dozen high frequency vibrations.<sup>52</sup> Including just one more vibrational mode in the spectral density increases the number of equations immensely. Thus, it is practically impossible to use a realistic spectral density, especially for large antenna complexes. Notice, however, that recent development in HE integration with graphics processing units (GPUs) has led to a huge improvement in computing time.<sup>34–36</sup> This allowed the modeling of linear and nonlinear (2D echo) responses for FMO complex with the spectral density including up to 11 vibrational modes.<sup>36</sup>

(7) In all the perturbative models, the exciton relaxation/migration (and delocalization of the exciton states) is independent of the phonon reorganization dynamics. In the Redfield picture, it is assumed that the reorganization energy is much less than the intermolecular coupling. In this case, the diabatic potential surfaces of the, for example, two different sites have small relative displacements along effective nuclear coordinates, so that the mixing of the two surfaces can be treated as uniform, i.e., independent of the nuclear coordinates. Relaxation between the thus mixed states is then also independent of the nuclear dynamics. In the case of bigger displacements, the superposition of the two states becomes essentially nonuniform, producing a strong mixing near the crossing point and more localized states near the bottom of the two potential surfaces. The phonon relaxation in such a

configuration gives rise to a so-called “dynamic localization”. This feature is included in the HE approach. In the SF approach, the excitations are always localized, implying nonmixed potential surfaces (their relative displacements can be arbitrarily large). Our analysis shows that the delocalization in the B800 ring is not significantly affected by the dynamic localization, being determined mostly by the disorder and thermal (incoherent) mixing of the exciton wave functions.

(8) Additional phonon-induced localization is connected with polaron effects emerging from a specific dependence of the displacement values on the excitation density. In this case, a nonuniformly delocalized exciton produces a nonuniform distribution of the displacements of the diabatic surfaces giving rise to an even more localized exciton wave function. Polaron effects are not included in the Redfield models and HE, but we suppose that these effects are not dominant in the B800 antenna where we found no significant discrepancies in modeling the excitonic spectra.

## 5. CONCLUSIONS

The B800 ring is an excellent example of a system where the interpigment coupling ( $\sim 20 \text{ cm}^{-1}$ ) is exactly in between the strong and weak coupling limit. In this region, the excitations are predominantly localized, but there are still some coherences, giving sizable contributions to the spectral responses. When using the localized (Förster) theory, one can obtain rather realistic population kinetics, but the coherences are omitted. On the other hand, in the Redfield picture, it is quite difficult to model the almost localized excitations in terms of the excitonic (delocalized) basis. To obtain the correct localized dynamics, one should describe very precisely a superposition of the exciton populations and the coherences between the exciton states (including nonsecular transfers between them). This is not included in a secular version of the standard Redfield and in the modified Redfield theory. In the full version of the standard Redfield, the nonsecular transfers are taken into account but only in terms of single-phonon transitions. The hierarchical equations method would be the best solution to the problem, but this method is numerically expensive.

In the present study of the B800 antenna, we demonstrate that the excitations in the B800 ring are localized due to static disorder and thermal effects, but there are still sizable excitonic effects producing shift, narrowing, and asymmetry of the OD spectra and the nonzero CD spectrum. The excitation dynamics reveals the presence of long-lived (about 1 ps) non-oscillatory coherences maintained due to nonsecular population-to-coherence transfers. Thus, we confirm the presence of a one-exciton coherence in the B800 ring giving an additional contribution to the induced absorption anisotropy as was suggested earlier.<sup>29</sup> According to present modeling, the motion of excitation around the ring occurs (on average) with a time constant of about 3–4 ps. This is slower than the B800  $\rightarrow$  B850 transfer, again in agreement with our earlier model<sup>29</sup> and recent 2D experiment.<sup>26</sup>

## ■ APPENDIX A. ONE-EXCITON DYNAMICS

### A1. Standard Redfield Equation

Supposing that the mixing of the electronic excitations is not dependent on the phonon coordinates, it is possible to switch to the exciton representation by diagonalization of the electronic Hamiltonian (eq 1). This will give us the new set

of energies  $\omega_{k0}$  corresponding to transitions from the ground to the  $k$ th exciton state, and the wavefunctions  $c_j^k$  giving the participation of the  $j$ th site in the  $k$ th exciton state. The excited-state dynamics is then given by the equation for the density matrix in the exciton representation:

$$\dot{p}_{kk'} = -i\omega_{kk'}p_{kk'} - \sum_{pp'} R_{kk'pp'} p_{pp'} \quad (\text{A1})$$

with the Redfield relaxation tensor:<sup>53,54</sup>

$$R_{kk'pp'} = -Y_{pkp'k'} - Y_{p'k'pk}^* + \delta_{p'k'} \sum_s Y_{pssk} + \delta_{pk} \sum_s Y_{p'ssk'}^* \\ Y_{kk'k''k'''} = \int_0^\infty dt e^{i\omega_{kk'}t} \int_{-\infty}^\infty \frac{d\omega}{2\pi} C_{kk'k''k'''}(\omega) \left[ \coth \frac{\omega}{2\theta} \cos \omega t - i \sin \omega t \right] \quad (\text{A2})$$

where indices  $k, p$ , and  $s$  number the exciton eigenstates,  $p_{kk}$  and  $p_{kk'}$  are the density matrix elements corresponding to populations and coherences in the exciton representation,  $\omega_{kk'} = \omega_{k0} - \omega_{k'0}$  is the energy gap between the two states (where the transition frequencies  $\omega_{k0}^0$  correspond to the zero-phonon lines), and  $C_{kk'k''k'''}(\omega)$  is the spectral density of electron–phonon coupling in the exciton representation:

$$C_{kk'k''k'''}(\omega) = \sum_j c_j^k c_j^{k'} c_j^{k''} c_j^{k'''} C_j(\omega) \quad (\text{A3})$$

where  $C_j(\omega)$  is the spectral density in the site representation. Notice the Redfield equation can include arbitrary spectral density  $C_j(\omega)$  and arbitrary temperatures. Initial conditions corresponding to excitation of the  $j$ th site are  $p_{kk'} = c_j^k p_{jj} c_j^{k'}$ . Notice that initial localization at one site corresponds to coherent excitation of several exciton states (by creating populations  $p_{kk}$  together with the coherences  $p_{kk'}$ ). After calculating the evolution of the exciton populations  $p_{kk}$  and coherences  $p_{kk'}$  according to eq A1, we can switch back to the site representations to obtain the kinetics of the site populations  $p_{ii} = c_i^k p_{kk} c_i^{k'}$  and site coherences  $p_{ij} = c_i^k p_{kk'} c_j^{k'}$ .

In eq A1, the phonons do not perturb the exciton wavefunctions but induce transfers between the exciton eigenstates. The rates of the transfers between one-exciton populations, between coherences, and population-coherence transfers (A2) are calculated supposing a weak coupling to phonons and treating the exciton–phonon interaction as a perturbation.

Sometimes the so-called secular approximation is used, keeping only the  $R_{kk'pp'}$  elements with  $\omega_{kk'} - \omega_{pp'} = 0$ . Notice that the dynamics of populations and coherences can change dramatically when switching from the full to secular  $R_{kk'pp'}$  tensor.

## A2. Modified Redfield Equation

The modified Redfield theory is restricted to one-exciton population transfers:

$$\dot{p}_{kk} = - \sum_{k'} R_{kkk'k} p_{k'k} \quad (\text{A4})$$

but the relaxation tensor is calculated supposing a more realistic description of the exciton–phonon coupling. More specifically,

the diagonal (in the exciton representation) part of exciton–phonon coupling is taken into account nonperturbatively, thus giving a realistic line shape for the exciton levels. The off-diagonal part (responsible for transitions between the exciton states) is treated as a perturbation. The exciton wavefunctions are still independent of the phonon coordinates, so the dynamic localization is not included. Moreover, the phonons are supposed to remain equilibrated during the electronic energy transfer. Under these assumptions, the relaxation tensor for  $k' \neq k$  is<sup>55</sup>

$$R_{kkk'k'} = -2 \operatorname{Re} \int_0^\infty dt \exp\{-i\omega_{kk'}t - i\lambda_{kkkk'}t - g_{kkkk'}(t) \\ - i\lambda_{k'k'k'k}t - g_{k'k'k'k}(t)\} \\ \exp\{2g_{k'k'kk}(t) + 2i\lambda_{k'k'kk}t\} \cdot [\dot{g}_{kk'k'k}(t) \\ - \{\dot{g}_{k'kkk'}(t) - \dot{g}_{k'kkk}(t) + 2i\lambda_{k'kkk'k}\} \\ \{\dot{g}_{k'k'kk'}(t) - \dot{g}_{kkkk'}(t) + 2i\lambda_{k'k'kk'k}\}] \\ g_{kk'k'k''}(t) = - \int_{-\infty}^\infty \frac{d\omega}{2\pi\omega^2} C_{kk'k'k''}(\omega) \left[ (\cos \omega t - 1) \coth \frac{\omega}{2\theta} - i(\sin \omega t - \omega t) \right] \\ \lambda_{kk'k'k''} = - \lim_{t \rightarrow \infty} \frac{d}{dt} \operatorname{Im}\{g_{kk'k'k''}(t)\} \\ = \int_{-\infty}^\infty \frac{d\omega}{2\pi\omega} C_{kk'k'k''}(\omega) \quad (\text{A5})$$

Here the transition frequencies correspond to the zero-phonon lines, i.e.,  $\omega_{kk'} = \omega_{k0}^0 - \omega_{k'0}^0$ . Notice that the energy of the Franck–Condon transition is  $\omega_{k0} = \omega_{k0}^0 + \lambda_{kkkk}$  where  $\lambda_{kkkk}$  is the reorganization energy in the exciton representation. For the spectral density given by eq 2,  $\lambda_{kkkk} = \sum_j \lambda_j (c_j^k)^4$ . If the coupling to phonons is weak, we can expand the transfer rate with respect to  $C_{kk'k'k''}$ . In first order, the modified Redfield formula A5 reduces to

$$R_{kkk'k'} = -2 \operatorname{Re} \int_0^\infty dt e^{-i\omega_{kk'}t} \ddot{g}_{kk'k'k}(t) \\ = -2 \operatorname{Re} \int_0^\infty dt e^{-i\omega_{kk'}t} \\ \int_{-\infty}^\infty \frac{d\omega}{2\pi} C_{kk'k'k}( \omega) \left[ \cos \omega t \coth \frac{\omega}{2\theta} - i \sin \omega t \right] \quad (\text{A6})$$

This transfer rate is the same as that in the standard Redfield theory (see eq A2). The diagonal elements of the Redfield tensor (corresponding to the lifetimes of the  $k$ th exciton level) are

$$R_{kkkk} = - \sum_{k' \neq k} R_{k'k'kk} \quad (\text{A7})$$

In the modified Redfield, these elements should be calculated by substituting eq A5 into eq A7, whereas in the standard Redfield the diagonal and off-diagonal elements follow from eq A2, so that the equality A7 is satisfied automatically.

## A3. Förster Equation

In the Förster theory, excitations are supposed to be localized at one site. The hopping-type motion between the sites is given by



$$\dot{p}_{jj} = -\sum_{j'} R_{jj'j'} p_{j'j'} \quad (\text{A8})$$

where  $p_{jj}$  are the site populations. The coupling of the localized electronic excitations to phonons is included nonperturbatively, whereas exciton couplings  $M_{jj'}$  (responsible for transfers between the  $j$ th and  $j'$ th sites) are treated as perturbation. The transfer rates can be expressed in the same form as in eq A5:<sup>50</sup>

$$\begin{aligned} R_{jj'j'} &= -2|M_{jj'}|^2 \operatorname{Re} \int_0^\infty dt \exp\{-i\omega_{jj'}t - i\lambda_j t - g_j(t) \\ &\quad - i\lambda_{j'}t - g_{j'}(t)\} \\ g_j(t) &= -\int_{-\infty}^\infty \frac{d\omega}{2\pi\omega^2} C_j(\omega) \left[ (\cos \omega t - 1) \right. \\ &\quad \left. \coth \frac{\omega}{2\theta} - i(\sin \omega t - \omega t) \right] \\ \lambda_j &= -\lim_{t \rightarrow \infty} \frac{d}{dt} \operatorname{Im}\{g_j(t)\} = \int_{-\infty}^\infty \frac{d\omega}{2\pi\omega} C_j(\omega) \end{aligned} \quad (\text{A9})$$

Here the transition frequencies correspond to the zero-phonon lines, i.e.,  $\omega_{jj'} = \omega_{j0}^0 - \omega_{j'0}^0$ . The energies of Frank–Condon transition are  $\omega_{j0} = \omega_{j0}^0 + \lambda_j$ , where  $\lambda_j$  is the reorganization energy in the site representation. Notice that eqs A9 and A5 are valid for arbitrary spectral density  $C_j(\omega)$ .

## ■ APPENDIX B. LINEAR SPECTRAL RESPONSES

### B1. Standard Redfield Theory

The first order equation for the density matrix in the exciton representation is

$$\dot{p}_{k0} = -i(\omega_{k0}^0 - \omega)p_{k0} - \sum_{k'} R_{k0k'} p_{k'0} + i d_{k0}^e \quad (\text{B1})$$

where  $p_{k0}$  is the coherence between the ground- and the  $k$ th one-excited state,  $\omega_{k0}^0$  is the corresponding energy of the zero-phonon transition,  $d_{k0}^e$  is a projection of the one-excited transition dipole to the field,  $R_{k0k'0}$  is the relaxation tensor that can be calculated using eq A2, as was shown in ref 52. The OD/CD spectra can be calculated similarly to eqs 5–7. The solution is greatly simplified in the secular approximation for the  $R_{k0k'0}$  tensor, meaning that the tensor is diagonal,  $R_{k0k0}$ :

$$\begin{aligned} \text{OD}(\omega) &= \frac{1}{3}\omega \sum_k \mathbf{d}_{k0}^2 \operatorname{Im}\{L_{k0}(\omega)\}; \quad \mathbf{d}_{k0} = \sum_j c_j^k \mathbf{d}_{j0} \\ \text{CD}(\omega) &= \frac{4}{3}k_\omega \omega \sum_k \mathbf{m}_{k0} \mathbf{d}_{k0} \operatorname{Im}\{L_{k0}(\omega)\}; \\ \mathbf{m}_{k0} &= \sum_j c_j^k [\mathbf{R}_j \mathbf{d}_{j0}] \\ L_{k0}(\omega) &= (\omega_{k0}^0 - \omega - iR_{k0k0})^{-1} \end{aligned} \quad (\text{B2})$$

where square brackets  $[\mathbf{R}_j \mathbf{d}_{j0}]$  denote the vector product.

We have found that the OD/CD spectra of B800 antenna calculated with the secular approximation (eq B2) and with the full  $R_{k0k'0}$  tensor (eq B1) are almost undistinguishable. Thus, we can use a secular approximation of the  $R_{k0k'0}$  tensor. However, we cannot do the same in modeling of the one-

exciton dynamics, where calculations with the secular or full relaxation tensor  $R_{kk'pp'}$  can give significantly different results!

### B2. Modified Redfield Theory

In the modified Redfield approach, the OD and CD spectra are<sup>52,55,56</sup>

$$\begin{aligned} \text{OD}(\omega) &= \frac{1}{3}\omega \sum_k \mathbf{d}_{k0}^2 \operatorname{Re} \int_0^\infty A(t) dt \\ \text{CD}(\omega) &= \frac{4}{3}k_\omega \omega \sum_k \mathbf{m}_{k0} \mathbf{d}_{k0} \operatorname{Re} \int_0^\infty A(t) dt \\ A(t) &= \exp\left\{i(\omega - \omega_{k0})t - g_{kkk}(t) - \frac{1}{2}R_{kkk}t\right\} \end{aligned} \quad (\text{B3})$$

where  $\omega_{k0} = \omega_{k0}^0 + \lambda_{kkk}$  is the energy of the Franck–Condon transition for the  $k$ th exciton state. The last term in the line shape function  $A(t)$  describes the relaxation/energy-transfer-induced broadening.

### B3. Förster Picture

In the localized (Förster) picture, the CD spectrum is equal to zero. The OD spectrum is

$$\begin{aligned} \text{OD}(\omega) &= \frac{1}{3}\omega \sum_j \mathbf{d}_{j0}^2 \operatorname{Re} \int_0^\infty A(t) dt \\ A(t) &= \exp\left\{i(\omega - \omega_{j0})t - g_j(t) - \frac{1}{2}R_{jjj}t\right\} \\ R_{jjj} &= -\sum_{j' \neq j} R_{j'j'jj} \end{aligned} \quad (\text{B4})$$

where  $\omega_{j0} = \omega_{j0}^0 + \lambda_j$  is the energy of the Franck–Condon transition for the  $j$ th site. The last term in the line shape function  $A(t)$  describes the migration-induced broadening.

## ■ AUTHOR INFORMATION

### Corresponding Author

\*E-mail: novoder@belozersky.msu.ru.

### Notes

The authors declare no competing financial interest.

## ■ ACKNOWLEDGMENTS

V.N. was supported by the Russian Foundation for Basic Research (Grant No. 12-04-01085). R.v.G. acknowledges financial support from a TOP grant (700.58.305) from the Foundation of Chemical Sciences and from an Advanced Investigator Grant (267333, PHOTPROT) from the European Research Council.

## ■ REFERENCES

- (1) McDermott, G.; Prince, S. M.; Freer, A. A.; Hawthornthwaite-Lawless, A. M.; Papiz, M. Z.; Cogdell, R. J.; Isaacs, N. W. Crystal Structure of an Integral Membrane Light-Harvesting Complex from Photosynthetic Bacteria. *Nature* **1995**, *374*, 517–521.
- (2) Koepke, J.; Hu, X.; Muenke, C.; Schulten, K.; Michel, H. The Crystal Structure of the Light-Harvesting Complex II (B800–850) from *Rhodospirillum rubrum*. *Structure* **1996**, *4*, 581–597.
- (3) Papiz, M. Z.; Prince, S. M.; Howard, T.; Cogdell, R. J.; Isaacs, N. W. The Structure and Thermal Motion of the B800–850 LH2 Complex from *Rps. Acidophila* at 2.0 Å Resolution and 100 K: New Structural Features and Functionally Relevant Motions. *J. Mol. Biol.* **2003**, *326*, 1523–1538.

- (4) Hu, X.; Ritz, T.; Damjanović, A.; Autenrieth, F.; Schulten, K. Photosynthetic Apparatus of Purple Bacteria. *Q. Rev. Biophys.* **2002**, *35*, 1–62.
- (5) van Grondelle, R.; Novoderezhkin, V. I. Energy Transfer in Photosynthesis: Experimental Insights and Quantitative Models. *Phys. Chem. Chem. Phys.* **2006**, *8*, 793–807.
- (6) van Grondelle, R.; Novoderezhkin, V. I. Spectroscopy and Dynamics of Excitation Transfer and Trapping in Purple Bacteria. In *The Purple Phototrophic Bacteria*; Hunter, C. N., Daldal, F., Thurnauer, M. C., Beatty, J. T., Eds.; Advances in Photosynthesis and Respiration, Vol. 28; Springer: Dordrecht, The Netherlands, 2008; Chapter 13, pp 231–252.
- (7) van der Laan, H.; Schmidt, Th.; Visschers, R. W.; Visscher, K. J.; van Grondelle, R.; Völker, S. Energy Transfer in the B800–850 Antenna Complex of Purple Bacteria *Rhodobacter Sphaeroides*: A Study by Spectral Hole-Burning. *Chem. Phys. Lett.* **1990**, *170*, 231–238.
- (8) Reddy, N. R. S.; Small, G. J.; Seibert, M.; Picorel, R. Energy-Transfer Dynamics of the B800-B850 Antenna Complex of *Rhodobacter Sphaeroides* – a Hole Burning Study. *Chem. Phys. Lett.* **1991**, *181*, 391–399.
- (9) de Caro, C. D.; Visschers, R. W.; van Grondelle, R.; Völker, S. Inter- and Intraband Energy Transfer in LH2-Antenna Complexes of Purple Bacteria. A Fluorescence Line-Narrowing and Hole-Burning Study. *J. Phys. Chem.* **1994**, *98*, 10584–10590.
- (10) Wu, H.-M.; Savikhin, S.; Reddy, N. R. S.; Jankowiak, R.; Cogdell, R. J.; Small, G. J. Femtosecond and Hole-Burning Studies of B800's Excitation Energy Relaxation Dynamics in the LH2 Antenna Complex of *Rhodospseudomonas Acidophila* (Strain 10050). *J. Phys. Chem.* **1996**, *100*, 12022–12033.
- (11) Matsuzaki, S.; Zazubovich, V.; Fraser, N. J.; Cogdell, R. J.; Small, G. J. Energy Transfer Dynamics in LH2 Complexes of *Rhodospseudomonas acidophila* Containing Only One B800 Molecule. *J. Phys. Chem. B* **2001**, *105*, 7049–7056.
- (12) Zazubovich, V.; Jankowiak, R.; Small, G. J. On B800-B800 Energy Transfer in the LH2 Complex of Purple Bacteria. *J. Lumin.* **2002**, *98*, 123–129.
- (13) Joo, T.; Jia, Y.; Yu, J.-Y.; Jonas, D. M.; Fleming, G. R. Dynamics in Isolated Bacterial Light Harvesting Antenna (LH2) of *Rhodobacter Sphaeroides* at Room Temperature. *J. Phys. Chem.* **1996**, *100*, 2399–2409.
- (14) Wendling, M.; Van Mourik, F.; Van Stokkum, I. H. M.; Salverda, J. M.; Michel, H.; Van Grondelle, R. Low-Intensity Pump-Probe Measurements on the B800 Band of *Rhodospirillum Molischianum*. *Biophys. J.* **2003**, *84*, 440–449.
- (15) Hess, S.; Feldchtein, F.; Babin, A.; Nurgaleev, I.; Pullerits, T.; Sergeev, A.; Sundström, V. Femtosecond Energy Transfer within the LH2 Peripheral Antenna of the Photosynthetic Purple Bacteria *Rhodobacter Sphaeroides* and *Rhodospseudomonas Palustris* LL. *Chem. Phys. Lett.* **1993**, *216*, 247–257.
- (16) Hess, S.; Åkesson, E.; Cogdell, R. J.; Pullerits, T.; Sundström, V. Energy Transfer in Spectrally Inhomogeneous Light-Harvesting Pigmentprotein Complexes of Purple Bacteria. *Biophys. J.* **1995**, *69*, 2211–2225.
- (17) Monshouwer, R.; Ortiz De Zarate, I.; Van Mourik, F.; Van Grondelle, R. Low-Intensity Pump-Probe Spectroscopy on the B800 to B850 Transfer in the Light Harvesting 2 Complex of *Rhodobacter Sphaeroides*. *Chem. Phys. Lett.* **1995**, *246*, 341–346.
- (18) Ma, Y. Z.; Cogdell, R. J.; Gillbro, T. Energy Transfer and Exciton Annihilation in the B800–850 Antenna Complex of the Photosynthetic Purple Bacterium *Rhodospseudomonas Acidophila* (Strain 10050). A Femtosecond Transient Absorption Study. *J. Phys. Chem. B* **1997**, *101*, 1087–1095.
- (19) Ma, Y. Z.; Cogdell, R. J.; Gillbro, T. Femtosecond Energy-Transfer Dynamics between Bacteriochlorophylls in the B800–820 Antenna Complex of the Photosynthetic Purple Bacterium *Rhodospseudomonas Acidophila* (Strain 7750). *J. Phys. Chem. B* **1998**, *102*, 881–887.
- (20) Kennis, J. T. M.; Streltsov, A. M.; Aartsma, T. J.; Nozava, T.; Ames, J. Energy Transfer and Exciton Coupling in Isolated B800–850 Complexes of the Photosynthetic Purple Sulfur Bacterium *Chromatium Tepidum*. The Effect of Structural Symmetry on Bacteriochlorophyll Excited States. *J. Phys. Chem.* **1996**, *100*, 2438–2442.
- (21) Kennis, J. T. M.; Streltsov, A. M.; Vulto, S. I. E.; Aartsma, T. J.; Nozava, T.; Ames, J. Femtosecond Dynamics in Isolated LH2 Complexes of Various Species of Purple Bacteria. *J. Phys. Chem. B* **1997**, *101*, 7827–7834.
- (22) Pullerits, T.; Hess, S.; Herek, J. L.; Sundström, V. Temperature Dependence of Excitation Transfer in LH2 of *Rhodobacter sphaeroides*. *J. Phys. Chem. B* **1997**, *101*, 10560–10567.
- (23) Ihalaainen, J. A.; Linnanto, J.; Myllyperkiö, P.; van Stokkum, I. H. M.; Ücker, B.; Scheer, H.; Korppi-Tommola, J. E. I. Energy Transfer in LH2 of *Rhodospirillum Molischianum*, Studied by Subpicosecond Spectroscopy and Configuration Interaction Exciton Calculations. *J. Phys. Chem. B* **2001**, *105*, 9849–9856.
- (24) Salverda, J. M.; Van Mourik, F.; Van Der Zwan, G.; Van Grondelle, R. Energy Transfer in the B800 Rings of the Peripheral Bacterial Light Harvesting Complexes of *Rhodospseudomonas Acidophila* and *Rhodospirillum Molischianum* Studied with Photon Echo Techniques. *J. Phys. Chem. B* **2000**, *104*, 11395–11408.
- (25) Agarwal, R.; Yang, M.; Xu, Q. H.; Fleming, G. R. Three Pulse Photon Echo Peak Shift Study of the B800 Band of the LH2 Complex of *Rps. Acidophila* at Room Temperature: A Coupled Master Equation and Nonlinear Optical Response Function Approach. *J. Phys. Chem. B* **2001**, *105*, 1887–1894.
- (26) Zigmantas, D.; Read, E. L.; Mančal, T.; Brixner, T.; Gardiner, A. T.; Cogdell, R. J.; Fleming, G. R. Two-Dimensional Electronic Spectroscopy of the B800–820 Light-Harvesting Complex. *Proc. Natl. Acad. Sci. U.S.A.* **2006**, *103*, 12672–12677.
- (27) Renger, Th.; May, V.; Kühn, O. Ultrafast Excitation Energy Transfer Dynamics in Photosynthetic Pigment-Protein Complexes. *Phys. Rep.* **2001**, *343*, 137–254.
- (28) Kühn, O.; Sundström, V. Energy Transfer and Relaxation Dynamics in Light-Harvesting Antenna Complexes of Photosynthetic Bacteria. *J. Phys. Chem. B* **1997**, *101*, 3432–3440.
- (29) Novoderezhkin, V.; Wendling, M.; Van Grondelle, R. Intra- and Interband Transfers in the B800-B850 Antenna of *Rhodospirillum Molischianum*: Redfield Theory Modeling of Polarized Pump-Probe Kinetics. *J. Phys. Chem. B* **2003**, *107*, 11534–11548.
- (30) Cheng, Y. C.; Silbey, R. J. Coherence in the B800 Ring of Purple Bacteria LH2. *Phys. Rev. Lett.* **2006**, *96*, 028103(1–4).
- (31) Georgakopoulou, S.; Frese, R. N.; Johnson, E.; Koolhaas, M. H. C.; Cogdell, R. J.; Van Grondelle, R.; Van Der Zwan, G. Absorption and CD Spectroscopy and Modeling of Various LH2 Complexes From Purple Bacteria. *Biophys. J.* **2002**, *82*, 2184–2197.
- (32) Ishizaki, A.; Fleming, G. R. Unified Treatment of Quantum Coherent and Incoherent Hopping Dynamics in Electronic Energy Transfer: Reduced Hierarchy Equation Approach. *J. Chem. Phys.* **2009**, *130*, 234111(1–10).
- (33) Ishizaki, A.; Fleming, G. R. Theoretical Examination of Quantum Coherence in a Photosynthetic System at Physiological Temperature. *Proc. Natl. Acad. Sci. U.S.A.* **2009**, *106*, 17255–17260.
- (34) Kreisbeck, C.; Kramer, T.; Rodríguez, M.; Hein, B. High-Performance Solution of Hierarchical Equations of Motions for Studying Energy-Transfer in Light-Harvesting Complexes. *J. Chem. Theory Comput.* **2011**, *7*, 2166–2174.
- (35) Hein, B.; Kreisbeck, C.; Kramer, T.; Rodríguez, M. Modelling of Oscillations in Two-Dimensional Echo-Spectra of the Fenna–Matthews–Olson Complex. *New J. Phys.* **2012**, *14*, 023018(1–20).
- (36) Kreisbeck, C.; Kramer, T. Long-Lived Electronic Coherence in Dissipative Exciton Dynamics of Light-Harvesting Complexes. *J. Phys. Chem. Lett.* **2012**, *3*, 2828–2833.
- (37) Zhu, J.; Kais, S.; Rebentrost, P.; Aspuru-Guzik, A. Modified Scaled Hierarchical Equation of Motion Approach for the Study of Quantum Coherence in Photosynthetic Complexes. *J. Phys. Chem. B* **2011**, *115*, 1531–1537.
- (38) Strumpfer, J.; Schulten, K. Light Harvesting Complex II B850 Excitation Dynamics. *J. Chem. Phys.* **2009**, *131*, 225101(1–9).

- (39) Yeh, S.-H.; Zhu, J.; Kais, S. Population and Coherence Dynamics in Light Harvesting Complex II (LH2). *J. Chem. Phys.* **2012**, *137*, 084110-9.
- (40) Strümpfer, J.; Schulten, K. Excited State Dynamics in Photosynthetic Reaction Center and Light Harvesting Complex I. *J. Chem. Phys.* **2012**, *137*, 065101(1–8).
- (41) Strümpfer, J.; Schulten, K. Open Quantum Dynamics Calculations with the Hierarchy Equations of Motion on Parallel Computers. *J. Chem. Theory Comput.* **2012**, *8*, 2808–2816.
- (42) Tretiak, S.; Middleton, C.; Chernyak, V.; Mukamel, S. Bacteriochlorophyll and Carotenoid Excitonic Couplings in the LH2 System of Purple Bacteria. *J. Phys. Chem. B* **2000**, *104*, 9540–9553.
- (43) Meier, T.; Chernyak, V.; Mukamel, S. Multiple Exciton Coherence Sizes in Photosynthetic Antenna Complexes Viewed by Pump-Probe Spectroscopy. *J. Phys. Chem. B* **1997**, *101*, 7332–7342.
- (44) Kühn, O.; Sundström, V. Pump-Probe Spectroscopy of Dissipative Energy Transfer Dynamics in Photosynthetic Antenna Complexes: A Density Matrix Approach. *J. Chem. Phys.* **1997**, *107*, 4154–4164.
- (45) Novoderezhkin, V.; Monshouwer, R.; Van Grondelle, R. Exciton (De)Localization in the LH2 Antenna of *Rhodobacter Sphaeroides* As Revealed by Relative Difference Absorption Measurements of the LH2 Antenna and the B820 Subunit. *J. Phys. Chem. B* **1999**, *103*, 10540–10548.
- (46) Novoderezhkin, V. I.; Van Grondelle, R. Physical Origins and Models of Energy Transfer in Photosynthetic Light Harvesting. *Phys. Chem. Chem. Phys.* **2010**, *12*, 7352–7365.
- (47) Yang, M.; Damjanović, A.; Vaswani, H. M.; Fleming, G. R. Energy Transfer in Photosystem I of Cyanobacteria *Synechococcus Elongatus*: Model Study with Structure-Based Semi-Empirical Hamiltonian and Experimental Spectral Density. *Biophys. J.* **2003**, *85*, 140–158.
- (48) Novoderezhkin, V. I.; Marin, A.; Van Grondelle, R. Intra- and Inter-Monomeric Transfers in the Light Harvesting LHCII Complex: the Redfield-Förster Picture. *Phys. Chem. Chem. Phys.* **2011**, *13*, 17093–17103.
- (49) Renger, T.; Madjet, M. E.; Knorr, A.; Müh, F. How the Molecular Structure Determines the Flow of Excitation Energy in Plant Light-Harvesting Complex II. *J. Plant Physiol.* **2011**, *168*, 1497–1509.
- (50) Yang, M.; Fleming, G. R. Influence of Phonons On Exciton Transfer Dynamics: Comparison of the Redfield, Förster, and Modified Redfield Equations. *Chem. Phys.* **2002**, *275*, 355–372.
- (51) Meier, T.; Zhao, Y.; Chernyak, V.; Mukamel, S. Polarons, Localization, and Excitonic Coherence in Superradiance of Biological Antenna Complexes. *J. Chem. Phys.* **1997**, *107*, 3876–3893.
- (52) Novoderezhkin, V.; Palacios, M.; Van Amerongen, H.; Van Grondelle, R. Energy-Transfer Dynamics in the LHCII Complex of Higher Plants: Modified Redfield Approach. *J. Phys. Chem. B* **2004**, *108*, 10363–10375.
- (53) Chernyak, V.; Minami, T.; Mukamel, S. Exciton Transport in Molecular Aggregates Probed by Time and Frequency Gated Optical Spectroscopy. *J. Chem. Phys.* **2000**, *112*, 7953–7963.
- (54) Dahlbom, M.; Minami, T.; Chernyak, V.; Pullerits, T.; Sundström, V.; Mukamel, S. Exciton-Wave Packet Dynamics in Molecular Aggregates Studied with Pump-Probe Spectroscopy. *J. Phys. Chem. B* **2000**, *104*, 3976–3983.
- (55) Zhang, W. M.; Meier, T.; Chernyak, V.; Mukamel, S. Exciton-Migration and Three-Pulse Femtosecond Optical Spectroscopies of Photosynthetic Antenna Complexes. *J. Chem. Phys.* **1998**, *108*, 7763–7774.
- (56) Mukamel, S. *Principles of Nonlinear Optical Spectroscopy*; Oxford University Press: New York, 1995.